Optical bound states in the continuum in periodic structures: mechanisms, effects, and applications

Jiajun Wang,[a,†] Peishen Li,[b,†] Xingqi Zhao,[a,†] Zhiyuan Qian,[b] Xinhao Wang,[a] Feifan Wang,[b] Xinyi Zhou,[b] Dezhuan Han,[c,*] Chao Peng,[b,*] Lei Shi,[a,d,e,f,*] and Jian Zi[a,d,e,f,*]

[a]State Key Laboratory of Surface Physics, Key Laboratory of Micro- and Nano-Photonic Structures (Ministry of Education) and Department of Physics, Fudan University, Shanghai, China
[b]State Key Laboratory of Advanced Optical Communication Systems and Networks, School of Electronics, Peking University, Beijing, China
[c]College of Physics, Chongqing University, Chongqing, China
[d]Institute for Nanoelectronic devices and Quantum computing, Fudan University, Shanghai, China
[e]Collaborative Innovation Center of Advanced Microstructures, Nanjing University, Nanjing, China
[f]Shanghai Research Center for Quantum Sciences, Shanghai, China

Abstract. Optical bound states in the continuum (BICs) have recently stimulated a research boom, accompanied by demonstrations of abundant exotic phenomena and applications. With ultrahigh quality (Q) factors, optical BICs have powerful abilities to trap light in optical structures from the continuum of propagation waves in free space. Besides the high Q factors enabled by the confined properties, many hidden topological characteristics were discovered in optical BICs. Especially in periodic structures with well-defined wave vectors, optical BICs were discovered to carry topological charges in momentum space, underlying many unique physical properties. Both high Q factors and topological vortex configurations in momentum space enabled by BICs bring new degrees of freedom to modulate light. BICs have enabled many novel discoveries in light–matter interactions and spin–orbit interactions of light, and BIC applications in lasing and sensing have also been well explored with many advantages. In this paper, we review recent developments of optical BICs in periodic structures, including the physical mechanisms of BICs, explored effects enabled by BICs, and applications of BICs. In the outlook part, we provide a perspective on future developments for BICs.

Keywords: bound state in the continuum; light trapping; topological charge; polarization vortex; momentum space; light field manipulation; photonic crystal slab; nanophotonics.

Received Nov. 30, 2023; revised manuscript received Jan. 15, 2024; accepted Jan. 25, 2024; published online Feb. 26, 2024.

1 Introduction

Bound states in the continuum (BICs) have recently aroused great research interest due to the ability to confine waves in open systems. The journey into the realm of BICs began with early theoretical insights into scattering resonances in quantum mechanics. In 1929, von Neumann and Wigner[1] proposed BICs to describe bound electric wave functions embedded in the continuum of propagating modes realized by specially constructed three-dimensional potential[2]. In later developments, BICs were further extended to other wave systems, such as the familiar acoustic waves[3–6], water waves[7–10], and electromagnetic waves[11–20]. Among them, BICs are especially actively studied in optical systems in recent years, accompanied by a large number of new discoveries and applications such as optical microcavities, lasers, and sensors.

In optical systems, bound states are usually defined in contrast with the propagating waves in free space. For optical BICs, they are mostly defined in extended structures, in which the extended directions are periodic. Then, optical modes can have

---

well-defined wave vectors $\mathbf{k}_\parallel$ in the extended structure plane with translational symmetry[21]. The optical BIC describes the optical mode of a certain $\mathbf{k}_\parallel$, which does not radiate along the direction without translational symmetry, in other words, confines light inside the continuum modes of free space. This light trapping property is the salient and most applied characteristic of optical BICs. In contrast, other optical modes surrounding this BIC are leaky to radiate light to the far field of free space. Such a radiated light wave in free space, whose $\mathbf{k}_\parallel$ keeps the same as the leaky optical mode due to the translational symmetry, usually is a plane wave and has a definite polarization state. The $\mathbf{k}_\parallel$-dependent polarization distribution forms a polarization field in momentum space. The study of the momentum-space polarization field reveals more topological properties of optical BICs. The optical BICs are discovered to be topological defects in momentum space, carrying topological charges defined by the winding major axes of polarization states surrounding BICs[22–24]. The vortex configurations of optical BICs bring new polarization degrees of freedom, promoting research in topological photonics and singular optics. Besides the conventional optical BICs with infinite lifetimes, it was also proposed that when perturbations are introduced to slightly break the original symmetry, BICs will then evolve to be quasi-BICs[25]. Quasi-BICs have the advantages of bound states and regular radiative modes: being radiative but also having high Q factors, and have been applied in some research such as nonlinear enhancement and lasing. With those explored properties, optical BICs have shown advantages and potential applications in manipulating light fields and modulating light–matter interactions. More discoveries and applications require further research and exploration.

In this paper, optical BICs (stated as BICs in later discussions) in periodic structures are comprehensively reviewed from the physical mechanisms, and explored novel effects to applications. In Section 2, we delve into the physical mechanisms of BICs from different physical perspectives. Firstly, we discuss the Friedrich-Wintgen (FW) BICs principle, elucidating the formation of BICs through coupling and interference. BICs are then categorized based on different FW origins. Secondly, utilizing the FW mechanism, we further explore BICs by considering two specific basis vectors separately: plane waves and Bloch waves. Thirdly, we incorporate a multipolar perspective to elucidate the radiation properties of BICs. Lastly, we discuss the topological properties of BICs based on the topological charges defined by the polarization distribution around BICs. We also describe BICs with multiple radiation channels, such as those exceeding the diffraction limit, proposing an underexplored research area. In Section 3, we focus on the effects enabled by BICs, summarizing the evolution and modulation methods through various parameter tunings. Quasi-BICs, as a crucial extension of conventional BICs, are clearly introduced and defined, holding significant promise for further application developments. Leveraging both the high Q factors and topological nature of BICs, we discuss light manipulations in both the near field and far field. Additionally, we describe light–matter interactions based on BICs from the perspectives of strong coupling and nonlinear enhancement. In Section 4, we summarize two main applications of BICs, namely, lasing and sensing, incorporating recent developments. Section 5 concludes with a summary of this review, offering an outlook to anticipate possible new discoveries and applications of BICs.

2 Physical Mechanisms

2.1 FW BICs in periodic photonic systems

2.1.1 General theory of FW BICs

In 1958, Feshbach developed a unified theory to study the resonances for the quantum scattering event in a reaction[26]. A Feshbach resonance occurs when the total energy of the two reactant particles in the entrance channel is approximately equal to that of a bound state in the closed channel. Later, H. Friedrich and D. Wintgen demonstrated the formation of BICs due to the interference of resonances belonging to different channels, and showed that it is a general feature of the coupled-channel Schrödinger equation with only one open channel[27]. When two resonances pass each other as a function of a continuous parameter, their coupling will cause an avoided crossing of the resonance positions. Meanwhile, the resonance width of the two states will also be tuned by their coupling and interference. At a specific value of the tuning parameter, the width of one resonance vanishes and hence it becomes a BIC.

For the leaky modes in periodic optical structures, similar results can be obtained based on the temporal coupled-mode theory[28,29]. To understand this mechanism, we can take a simple two-level system as an example, which can be described by an effective non-Hermitian Hamiltonian[28,30]:

$$H = \begin{pmatrix} \omega_1 & \kappa \\ \kappa & \omega_2 \end{pmatrix} + i \begin{pmatrix} \gamma_1 & \pm\sqrt{\gamma_1\gamma_2} \\ \pm\sqrt{\gamma_1\gamma_2} & \gamma_2 \end{pmatrix}, \tag{1}$$

where ω_1 and ω_2 are the resonant frequencies of two modes, γ_1 and γ_2 are the decay rates, and κ and $\pm\sqrt{\gamma_1\gamma_2}$ are the near-field coupling and the far-field interference coefficients, respectively. When these parameters satisfy the condition

$$\kappa(\gamma_1 - \gamma_2) = \pm\sqrt{\gamma_1\gamma_2}(\omega_1 - \omega_2), \tag{2}$$

the decay rate of one mode vanishes. Therefore, this mode becomes a bound state, and the other mode will have a larger decay rate. This mechanism based on the tuning of near-field coupling and the far-field interference between two resonance modes is the origin of FW BICs.

We note that the imaginary part of the Hamiltonian in Eq. (1) is rank-deficient; there always exists a null vector $|\psi_0\rangle \propto (\sqrt{\gamma_2}, \mp\sqrt{\gamma_1})$ satisfying

$$H_{\text{imag}}|\psi_0\rangle = 0. \tag{3}$$

If $|\psi_0\rangle$ is also an eigenvector of H_{real}, i.e.,

$$H_{\text{real}}|\psi_0\rangle = \omega_0|\psi_0\rangle, \tag{4}$$

the state $|\psi_0\rangle$ is a BIC having a purely real eigenenergy and satisfying $H|\psi_0\rangle = \omega_0|\psi_0\rangle$. It is the constraint of Eq. (4) that gives rise to a relation between the near-field coupling and the far-field interference coefficients shown in Eq. (2). It is worth noting that the BIC condition only requires that H_{real} and H_{imag} share an eigenvector $|\psi_0\rangle$. However, for the two-level system, this condition will lead to the commutation relation $[H_{\text{real}}, H_{\text{imag}}] = 0$. This commutation relation, together with

H_{imag} being rank-deficient, is the sufficient condition for the existence of BICs.

2.1.2 Classification of BICs and their FW origins

According to their different characteristics, BICs in periodic structures are usually classified into three types. The first type is the original FW BIC, which is located near the avoided crossing points of the two bands and therefore can be clearly explained by the FW mechanism[31–35]. For example, in a one-dimensional plasmonic grating, the FW BICs can be found at the avoided crossings[32], as is shown in Fig. 1(a). Especially, when two modes are identical but separated in space, the occurrence of BIC can be achieved by controlling the optical path between these two modes. These two coupled modes in fact act as a Fabry-Perot cavity, and therefore the resultant BIC is named Fabry-Perot BICs, which can emerge in the structure of two identical PhC slabs arrayed in parallel[12].
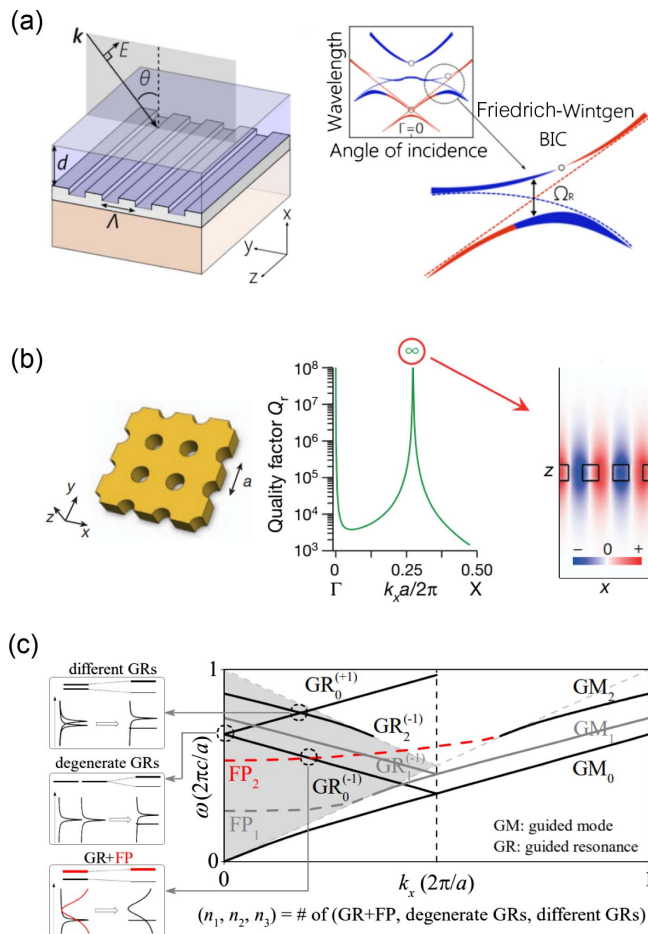

Fig. 1 Representative examples of different types of BICs in periodic photonic systems. (a) Original FW BICs and symmetry-protected BICs in one-dimensional plasmonic gratings. The original FW BICs appear at the avoided crossing points and symmetry-protected BICs appear at the Γ point[32]. (b) Accidental BIC supported by a PhC slab. It is located at the off-Γ point with the infinite Q factor and confined field profile[15]. (c) General descriptions of BICs in periodic photonic structures from the mechanism of FW BICs. Both the symmetry-protected BICs and accidental BICs have similar FW origins from the couplings of modes[44].

The second type is known as the symmetry-protected BIC, which is located at the center of momentum space (Γ point) and is guaranteed by the structural symmetry[36,37]. In structures with sufficient high in-plane symmetries, this type of BIC has been extensively investigated[32,34,38–41]. For instance, the structure in Fig. 1(a) has C_{2v} symmetry, which can support the symmetry-protected BICs. Since the plane waves outside are odd under the 180° rotation around the x axis (C_2), if the modes in the structure are even under C_2, they are incompatible with the plane waves outside. Thus, these modes will not couple to free space and turn into BICs.

Besides, a PhC slab can also support BICs that neither are protected by symmetry nor located near the avoided crossing points of two bands, as is shown in Fig. 1(b)[15]. This type of BIC seems to emerge from a single-resonance mode, called accidental BICs[15,23,24,33,42,43]. With the variations of structural parameters, accidental BICs remain robust and will not be destroyed. However, in contrast to symmetry-protected BICs, which are fixed at the Γ point, the wave vectors of accidental BICs will evolve in momentum space with the changes in structural parameters.

In periodic optical structures, the above three different types of BICs commonly exist and have been widely investigated. Actually, although these types of BICs appear to have different features, they can be uniformly described using the FW BIC mechanism[44]. In a PhC slab, there are in fact two types of modes located within the light cone: the guided resonances (GR) and Fabry-Perot (FP) modes, as is shown in Fig. 1(c). There are three different ways to achieve BICs through the coupling of these GR and FP modes. When two different GRs couple with each other at the off-Γ point and satisfy the FW BIC condition, an original FW BIC will occur in the vicinity of the avoided crossing point. Besides, the symmetry-protected BIC at the Γ point can be considered as a result of the coupling of degenerate GR modes. At the Γ point, the folded bands of guided modes give rise to a pair of degenerate states. When this pair of degenerate states is coupled to each other, one of them has a doubled radiation loss while the other becomes the symmetry-protected BIC. Different from the aforementioned two types, the accidental BICs originate from the coupling between GR and FP modes, occurring near the avoided crossing points of them. However, the FP modes were mostly considered only as the background of the spectrum because of their low Q factors. Therefore, the FW origin of accidental BICs is less obvious, often leading to their classification as single-resonance modes.

2.2 Plane-wave and Bloch-wave perspective of BICs

By choosing two specific quasi-modes as the basis vectors, the interference of modes gives a clear physics picture of BICs based on the FW mechanism. On the other hand, to explore other properties of BICs, there are also other alternative bases, such as plane waves or Bloch waves[45–48]. These choices are beneficial in facilitating a more rigorous derivation based on the first principles and more efficient computational methods to study BICs.

By treating the GRs in PhC slabs as the combination of a series of plane waves, the origin of BICs can be derived from an analytical iterative method[45]. The in-plane coupling caused by the permittivity periodicity and the surface coupling caused by the discontinuities at dielectric interfaces lead to the coupling
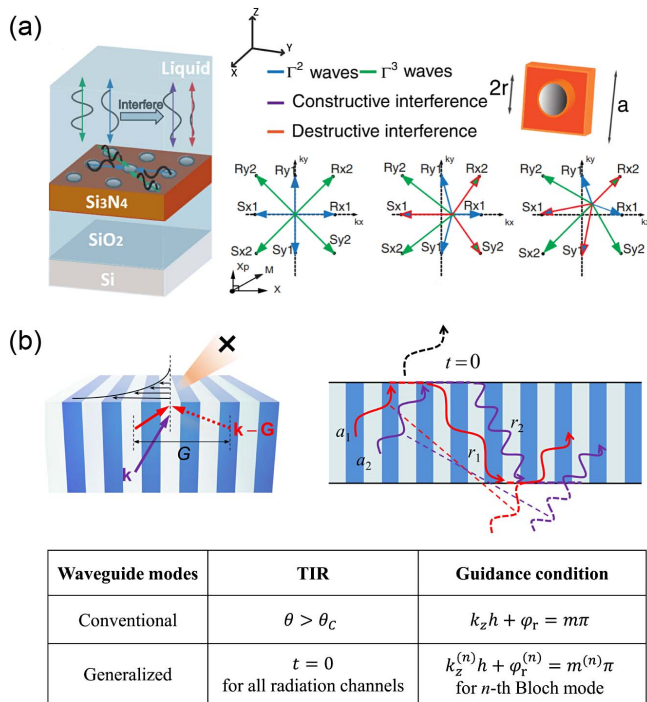
Fig. 2 Understandings of BICs from different bases: plane waves and Bloch waves. (a) Plane-wave perspective of BICs in PhC slabs[45]. Left: schematic view of a PhC slab with C_{4v} and up-down mirror symmetries. Right: participating channels of symmetry-protected BIC at the Γ point and accidental BICs along the $\Gamma - X$ and $\Gamma - M$ directions. (b) Mechanisms of BICs based on the total internal reflection of Bloch waves[48]. Upper left: schematic view of the TIR at the interface between the PhC slab and free space. Upper right: BIC in a PhC slab when both the TIR and phase accumulation conditions are satisfied. Lower: BICs and the generalized conditions for waveguide modes.

between different plane waves. As is shown in Fig. 2(a), for the symmetry-protected BICs, all of the coupling coefficients are symmetric, leading to complete destructive interference. Besides, for the off-Γ accidental BICs, by incorporating the radiation from all possible channels, the weighted destructive interference can cause the overall radiation to be suppressed.

The plane waves serve as a commonly used basis in numerical analysis. In comparison, the Bloch waves, as another kind of extended wave, contain the complete information from the in-plane periodicity and the formation of BICs can be interpreted by utilizing this basis[48]. For any optical mode in a PhC slab, it can be regarded as the superposition of some bulk Bloch waves of an infinite PhC. Then, the formation of BICs can be understood by the total internal reflection (TIR) of Bloch waves. As shown in Fig. 2(b), when the total transmission for an optical mode consisting of multiple Bloch waves from the PhC slab side to the free-space side vanishes, the TIR will occur. For a PhC slab, another condition to form the BICs is that the accumulated phase change of each Bloch wave should be an integer multiple of 2π for traveling a round trip, which is similar to that of a waveguide mode [lower panel of Fig. 2(b)]. When both the TIR and the phase accumulation conditions are satisfied, light can be perfectly guided in the slab, namely, forming a BIC. Since the Bloch waves can well depict the periodicity of PhC

slabs, the convergence speed for finding the BICs can be significantly enhanced by using this basis.

2.3 Multipolar perspective of BICs

As a powerful approach to understanding complicated electromagnetic fields from a local source, multipole expansion is extensively used to analyze the properties of optical systems[49]. In periodic structures, the overall optical properties can be regarded as the interferences of radiations from all the local sources: unit cells. For each unit cell, its radiation pattern can be decomposed by a series of multipoles. Through this method, insight can be gained into the underlying mechanisms that give rise to the non-radiative behavior of BICs, which is analogous to that for the existence of the Brewster angle for TM waves: the excited electric dipoles are aligned parallel to the direction of reflection.

It is well known that there are some directions (poles) along which the multipole's radiation vanishes. Actually, this inherent property of multipoles shares an intimate connection with the concept of BICs. In Fig. 3(a), the examples of the radiation patterns of both symmetry-protected BICs and accidental BICs are exhibited[50]. For the symmetry-protected BICs, they can be decomposed by a series of multipoles whose radiations vanish in the vertical direction. These multipole components are composed of a dominant component and other minor components. The dominant component will determine the properties of the modes, and its singularity index is closely associated with the topological charge of the BIC. To find BICs with high-order topological charges, multipole components of a high singularity index are required. It is worth noting that if the radiation is represented by a dominant individual multipole, then it is not possible to obtain a positive topological charge larger than $+1$[50]. For accidental BICs, the combinations of multipoles sum up to zero in a particular direction, as schematically shown in Fig. 3(b)[51]. When the accidental BIC moves in momentum space with the variation of structural parameters, the multipolar composition will change accordingly so that the multipolar singularity appears in a new direction[50,51].

Not limited to BICs, the multipole expansion can also be employed to characterize other types of singularities, such as unidirectional guided resonances or even the quasi-BICs in non-periodic systems[52–54]. For example, a photonic quasicrystal slab with eightfold rotational symmetry can also support modes with similar properties to BICs[53]. At the Γ point, a single mode is the center of a polarization vortex with a high Q factor, which is similar to the BICs in the periodic case. The far-field radiation patterns of these modes can by represented by multipoles, as is shown in Fig. 3(c). The topological charges of the vortices also have a direct correspondence to the indices of major dominant multipoles.

2.4 Topological perspective of BICs

For the modes located within the light cone in a PhC slab, they are leaky and can radiate to free space except for BICs. In general, the far-field radiations of these modes are elliptically polarized plane waves. The polarization states can be described by a vector $\boldsymbol{c} = (c_x, c_y)$, where c_x and c_y are the projected x and y components of the electric field, as is shown in Fig. 4(a). For a BIC, it does not radiate and therefore both components of the far-field radiation vanish, i.e., $c_x = c_y = 0$. With the undefined far-field polarization, a BIC is naturally a polarization
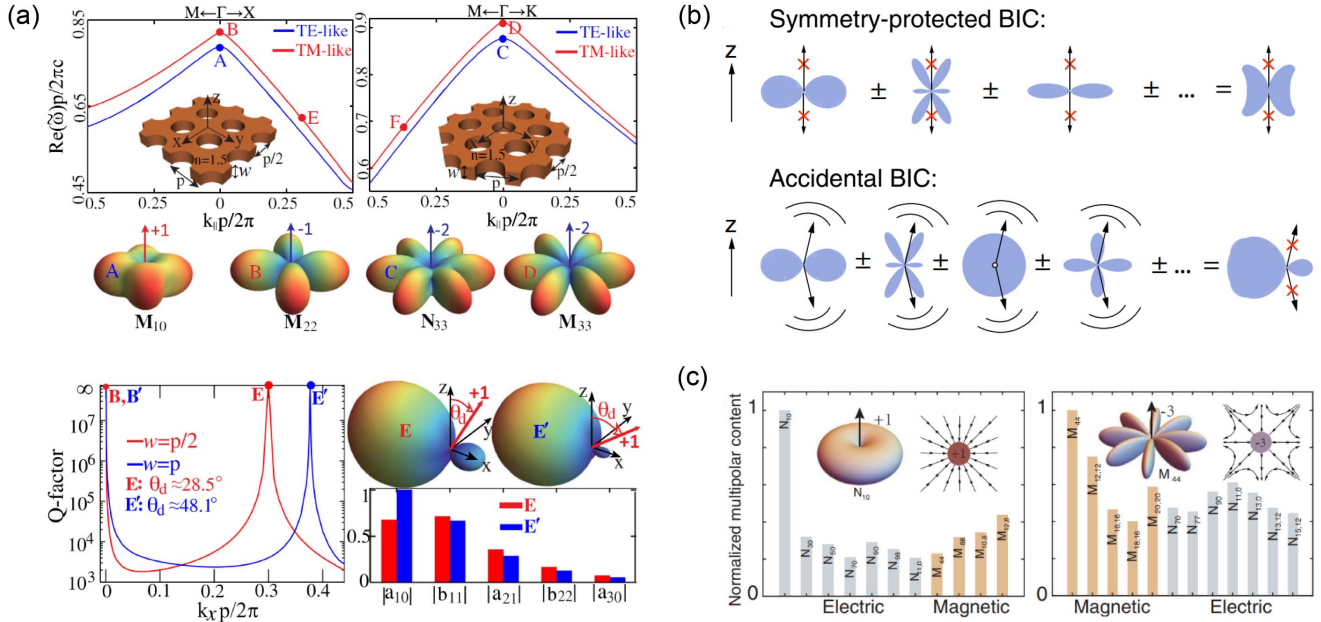
Fig. 3 Understandings of BICs from the perspective of multipolars. (a) Upper panel: radiation patterns and the dominant multipolar components of the symmetry-protected BICs in square and hexagonal PhCs. Lower panel: Q factor, far-field radiation patterns, and the major multipolar compositions of the accidental BICs[50]. (b) Schematic view of the multipolar origin of symmetry-protected and accidental BICs[51]. (c) Radiation patterns and multipolar components of the polarization vortices in photonic quasicrystals[53].

singularity in momentum space[22]. In the vicinity of a BIC, the polarization states will wind around it, forming a momentum-space polarization vortex. This winding nature can be characterized by the topological charge q, which is defined by

$$q = \frac{1}{2\pi} \oint_L d\mathbf{k} \cdot \nabla_k \phi(\mathbf{k}), \tag{5}$$

where L is a closed path around a BIC and $\phi(\mathbf{k})$ is the azimuthal angle of the polarization states' major axis. The topological charge of a BIC is an integer, which describes how many times the polarization states wind around the BIC in the counterclockwise direction. As a topological invariant, the topological charge is conserved during a continuous parameter variation, which is closely associated with various evolutions of polarization singularities in momentum space such as the merging, annihilation, and splitting of BICs.

This topological nature of BICs has been subsequently verified in experiments[23,24]. In a photonic crystal slab with C_{4v} symmetry, the vortex configurations of BICs were measured as shown in Fig. 4(b). The structure supports both the symmetry-protected BIC at the Γ point and the accidental BICs along the $\Gamma - X$ direction. In the measured extinction spectra, the excitations of resonance modes will lead to peaks, which can be ascribed to the radiation of excited modes. Since the BICs cannot couple with any external waves, they manifest as the vanished width of a peak in the spectra. From the polarization-dependent spectra, the polarization states of modes were further extracted. Around each BIC, the polarization states form a polarization vortex. The vortex configurations around BICs are also experimentally observed in a one-dimensional grating

[Fig. 4(c)], where two off-Γ BICs are located on the TM band and each BIC carries a $+1$ topological charge. In the reflectance spectra, the BICs are characterized as the vanished regions. Around a BIC, the orientation angle of the polarization states' major axis flips quadrants four times, indicating a 2π rotation and the $+1$ charge.

For the symmetry-protected BICs at the Γ point, the topological charges are also restricted by the symmetry of the structure. Each symmetry-protected BIC corresponds to an irreducible representation of the symmetry group[56], and thus its possible topological charge will be determined. Especially for the degenerate case, paired symmetry-protected BICs can be supported by structure with C_6 symmetry, corresponding to its E_2 representation[41]. Here, we listed all the possible topological charges of the symmetry-protected BICs in structures with different rotational symmetries, as is shown in Table 1. For example. the topological charge of the symmetry-protected BIC in Fig. 4(a) is -1 and it corresponds to the B representation of the C_4 symmetry group[22,23]. For the structure with C_6 symmetry, it can support symmetry-protected BIC with -2 charge[40,57]. However, BICs with higher topological charges still lack reporting.

Based on the graph theory, more non-local properties of the BICs in momentum space can be revealed[55]. As is shown in the left panel of Fig. 4(d), the topological charge for an arbitrary bounded face in the polarization graph is demonstrated to be zero, manifesting the correlation of polarization singularities in different positions. By utilizing this property, the polarization graph will provide a way to find undiscovered BICs that exist off the high-symmetry lines (general BICs). Besides, this type of BIC will evolve with the polarization graph when continuously varying the geometrical parameters. For example, on the right
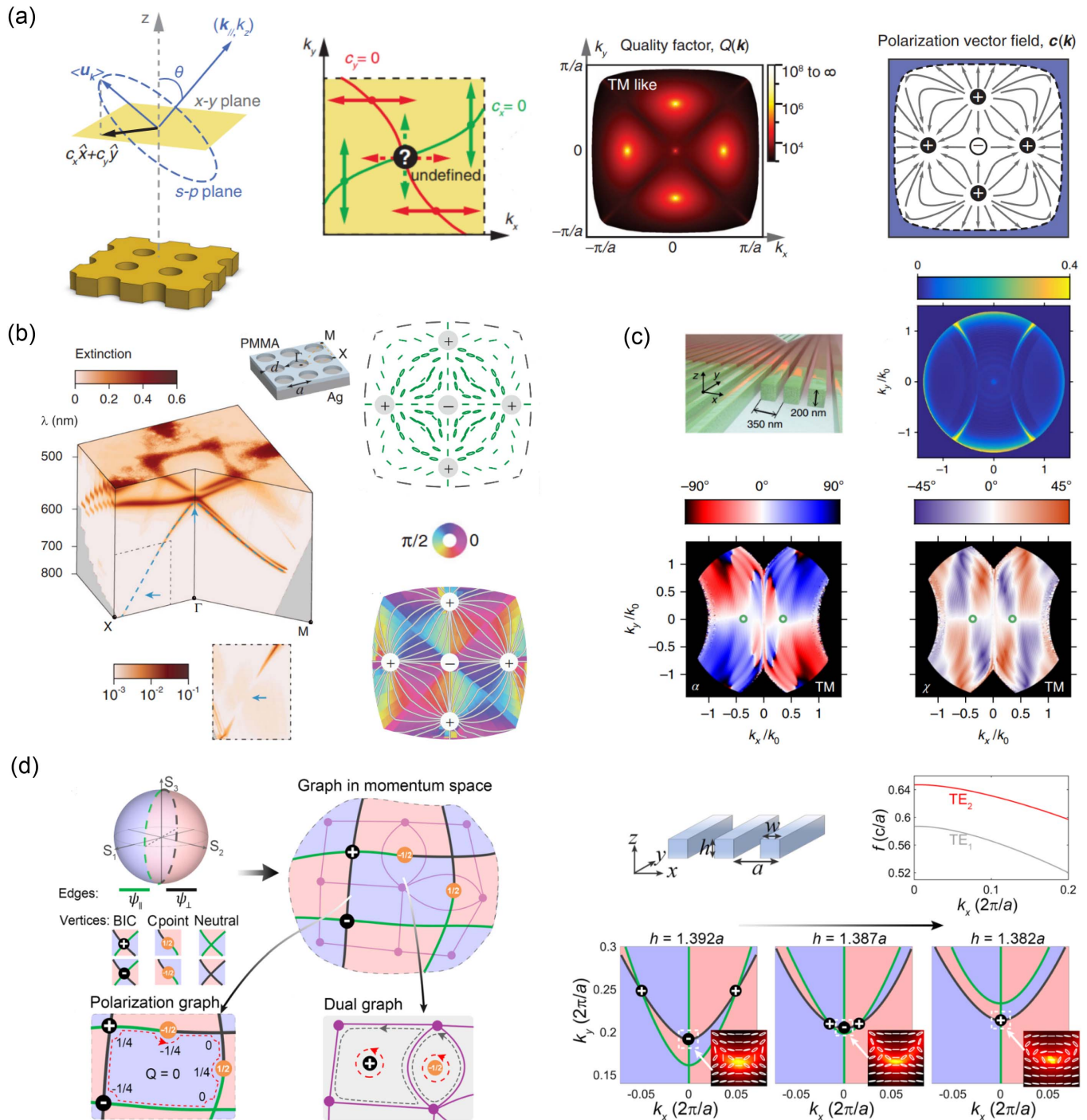
Fig. 4 Topological nature of BICs. (a) Topological nature of BICs[22]. First panel: schematic view of the far-field radiations of guided resonances in PhC slabs. Second panel: undefined far-field polarization of a BIC and the polarization vortex around it. Last two panels: distribution of Q factor and polarization vector in momentum space. (b), (c) Experimental observation of the polarization vortices around BICs in a C_{4v} photonic crystal slab[23] and a one-dimensional grating[24], respectively. (d) Left: polarization graph in momentum space. Right: merging of two general BICs and an off-Γ BIC with the variation of geometrical parameters[55].

panel of Fig. 4(d), the polarization graphs of a one-dimensional grating are exhibited. By decreasing the thickness of the grating, two general BICs gradually approach the off-Γ BIC on the k_y axis, and merge to remain an off-Γ BIC with charge $+1$.

2.5 BICs with multiple radiation channels

When a resonance mode has more than one independent radiation channel, the BIC condition requires that all the channels are inhibited. An example of multi-radiation channels is a mode

Table 1 Possible Topological Charges of the Symmetry-Protected BICs ($n = 0, \pm1, \pm2,...$ is an integer)

Symmetry	Representation	Charge	Allowed Charge
C_2	A	$2n + 1$	$\pm1, \pm3, \pm5, ...$
C_3	A	$3n + 1$	$+1, -2, +4, ...$
C_4	A	$4n + 1$	$+1, -3, +5, ...$
	B	$4n - 1$	$-1, +3, -5, ...$
C_6	A	$6n + 1$	$+1, -5, +7, ...$
	B	$6n - 2$	$-2, +4, -8, ...$
	E_2	$6n - 2$	$-2, +4, -8, ...$

beyond the diffraction limit[48,58,59]. For this case, the far-field radiation of a mode is a combination of plane waves containing more than one diffraction order. For example, the modes in a PhC slab can have two radiation channels, as is shown in Fig. 5(a)[48]: the zero-order diffraction and the −1st-order diffraction. A multi-channel BIC occurs when both the radiations of the two channels vanish. For each channel, the BIC is the center of the polarization vortex, while the topological charges of the zero-order diffraction is +1 and the −1st-order diffraction

is −1. When the thickness of the PhC slab is slightly varied, the behaviors of the two channels are different. For the zero-order diffraction, the polarization vortex with charge +1 will split into two half-integer charges of 1/2. For the −1st-order diffraction, the topological vortex persists.

The discussion of multi-channel BICs can be extended to modes located at the corner of the first Brillouin zone[59]. In a photonic crystal slab composed of a honeycomb array of cylindrical holes [Fig. 5(b)], the K point actually has three radiation channels. For leaky modes at the K point, the zero-order and the two first-order diffractions lead to three propagating waves in free space. By choosing appropriate geometric parameters, a BIC located at the K_1 point can be realized. Different from at-Γ BICs, the K-point BIC is not a symmetry-protected BIC, and it will be destroyed and spawn two C points when the geometric parameters are altered.

For modes below the diffraction limit, although only the zero-order diffraction is the propagating wave in free space, sometimes they can also be treated as multi-channel modes. For example, when the up-down mirror symmetry of a PhC slab is broken, the upward radiation and downward radiation of a mode are independent of each other. Therefore, they can be considered as two radiation channels. When one channel is suppressed while the other is still radiative, a unidirectional guided resonance (UGR) is realized[60,61]. Different from BICs, the UGRs radiate only towards one side of a PhC slab. The relations between UGRs and BICs will be discussed in Section 3.1 in detail.

3 Explored Effects Enabled by BICs

3.1 Evolution rules and modulation methods

BICs can be easily found in periodic photonic structures with certain rotational symmetry. The modulation methods and evolution rules of BICs are important research topics for the possible applications. With explored physical mechanisms of BICs, many approaches are proposed to modulate BICs in momentum space. Among them, changing the structural parameters is usually applied to modulate BICs.

By tuning the periodicity of the structures, multiple BICs can merge in momentum space[39] [Fig. 6(a)]. The closely distributed BICs allow a large area around Γ point with high Q factors, leading to a lower decay rate (from $\frac{1}{k^2}$ to $\frac{1}{k^6}$). Although the BICs theoretically have infinite Q factors, the inevitable scattering losses due to imperfect fabrications in the practical samples will limit the realized Q factors. From this perspective, the enhanced Q factors of all nearby resonances in the same band can strongly suppress the out-of-plane-scattering losses. It should be noted that when BICs with opposite charges merge and annihilate each other at Γ point, the Q factor decay rate will go back to the case of the isolated BIC ($\frac{1}{k^2}$).

By tuning the thickness of the structures, the BIC merging was also studied at the off-Γ region by Kang *et al.*[33] [Fig. 6(b)]. Compared with the original BIC, the merging BICs lead to the enhancement of Q factors around the merging center. This proposal offers approaches to designing high-Q optical modes at the off-Γ region. The experimental observation of BICs' merging at the off-Γ point was then reported by Hu *et al.*[44] [Fig. 6(c)]. In this work, by changing the etching depth h_g of the 1D PhC slab (the effective thickness is hence changed), the two BICs gradually move close to and merge with each other,
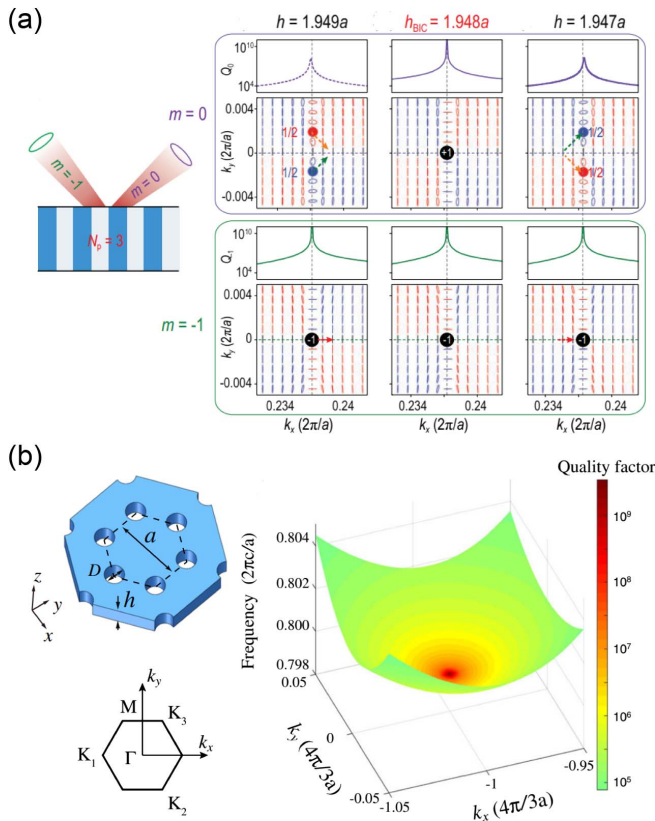

Fig. 5 BICs with multi-radiation channels. (a) BICs with two different radiation channels and the evolutions of the far-field polarization. Each radiation channel has a different behavior with the variation of structural parameters[48]. (b) Left: honeycomb-lattice photonic crystal slab and its first Brillouin zone. Right: distribution of the Q factor around a BIC at the K_1-point. The BIC has a divergent Q factor[59].
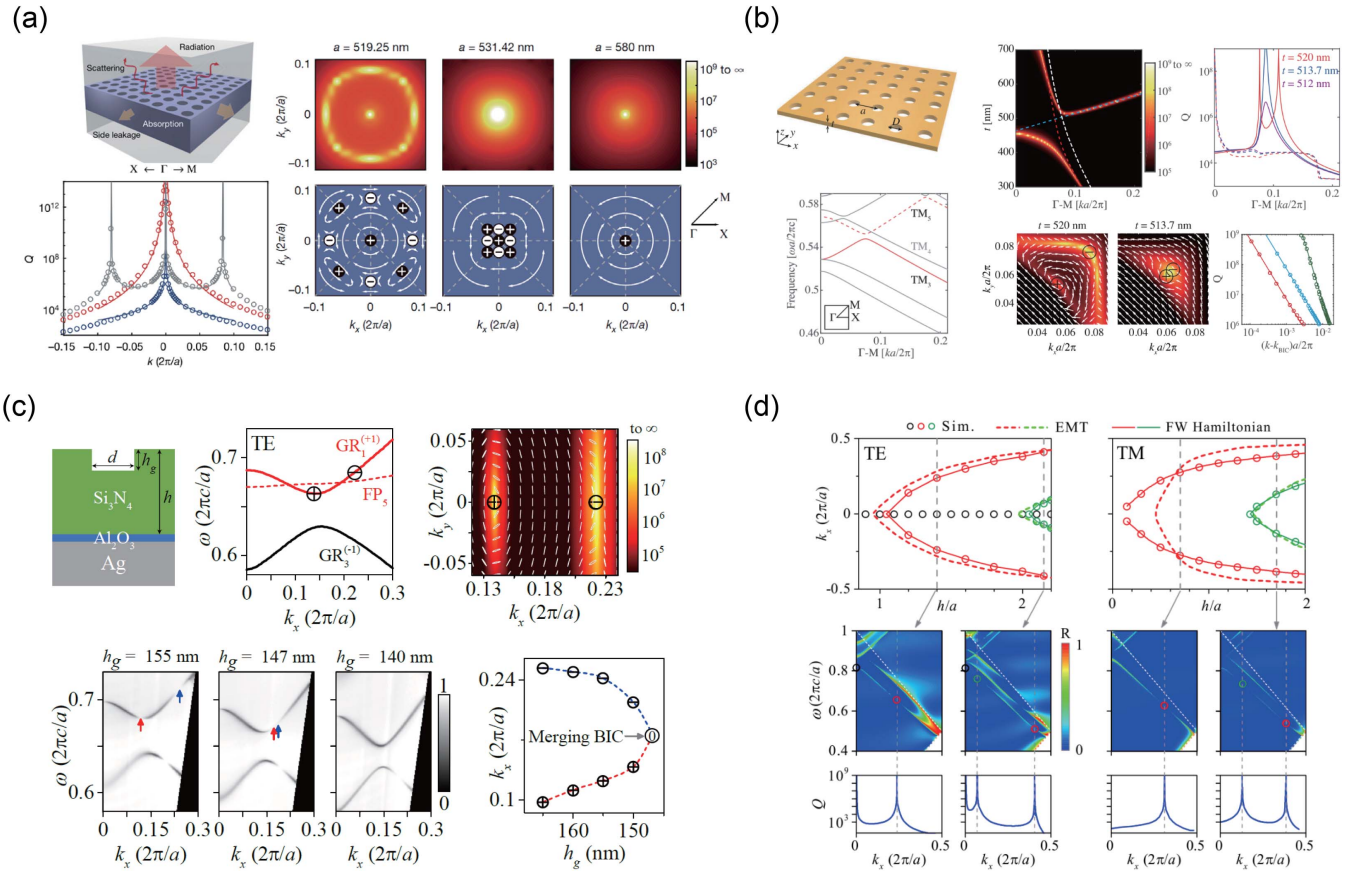
Fig. 6 Momentum-space evolution of BICs. (a) Merging process of multiple BICs by tuning the periodicity *a* of the structures[39]. As *a* increases, multiple BICs merge close to Γ point and BICs with opposite charges finally annihilate each other. (b) Merging process of two BICs with opposite charges by tuning the thickness *t* of the structures[33]. (c) Experimental observation of BIC merging at off-Γ point by tuning the etching depth h_g of the 1D PhC slab[44]. (d) Evolution of BICs in the $k_x - h$ space[44]. By continuously tuning the thickness *h*, the accidental BICs can continuously move along the photonic bands.

and then are annihilated at the off-Γ point. Besides, based on the FW mechanism of accidental BICs, the work also proposed and demonstrated that by tuning the structural thickness, the FP mode can be shifted in the frequency range; hence the accidental BICs can move along with the FP modes to exist at any k_x [Fig. 6(d)].

Besides periodicity and thickness, the proportion of different constituents in a unit cell is also the usually applied parameter. For example, by tuning the diameter of cylindrical holes in a dielectric slab, BICs are reported to exist at K points of a honeycomb-lattice PhC slab[59]. In these parameters' tuning, the original structural symmetries are maintained, and related evolutions have also been discussed in other studies[48,62–65]. When the structural symmetry degrees of freedom are further introduced, more evolution effects can be induced.

By breaking the in-plane inversion (C_2) symmetry, the at-Γ BIC with a topological charge ± 1 at Γ point was reported to split into a pair of *C* points, whose far-field radiations are circularly polarized[66]. From the perspective of singular optics, the BICs are actually null-amplitude points in the far field, which can be viewed as the result of collisions between *C* points and *L* lines (lines of linearly polarized states). Then when the BICs are destroyed by symmetry breaking, *C* points may spawn during

this process. For example, when changing the holes from squares to isosceles triangles, the BIC with topological charge $+1$ will split into a pair of *C* points with topological charge $+\frac{1}{2}$ [Fig. 7(a)]. The existence of *C* points was directly observed by measuring the transmittance spectra under circularly polarized incidence. The work also proposed that by this means full coverage on the Poincaré sphere can be realized accompanied by the appearance of *C* points. Note that the up-down mirror symmetry is not necessary; similar evolutions are also realized and applied in structures without up-down mirror symmetry[67–71].

Furthermore, when considering BICs with high-order topological charges, there are more possibilities to break the structural symmetries, giving rise to more various evolutions[40,57,62]. For example, the BIC with topological charge -2 can be easily found at Γ point in structures with C_{6v} symmetry. Figure 7(b) exhibits two types of typical evolution cases: when breaking the symmetry from C_{6v} to C_{2v}, the at-Γ BIC with topological charge -2 will be split into two off-Γ BICs with topological charge -1. When breaking the symmetry from C_{6v} to C_{3v}, the at-Γ BIC with topological charge -2 will be split into six off-Γ *C* points with topological charge $-1/2$ and one at-Γ BIC with topological charge $+1$. When further breaking the symmetry into C_{1h}, more evolution possibilities were theoretically discussed by
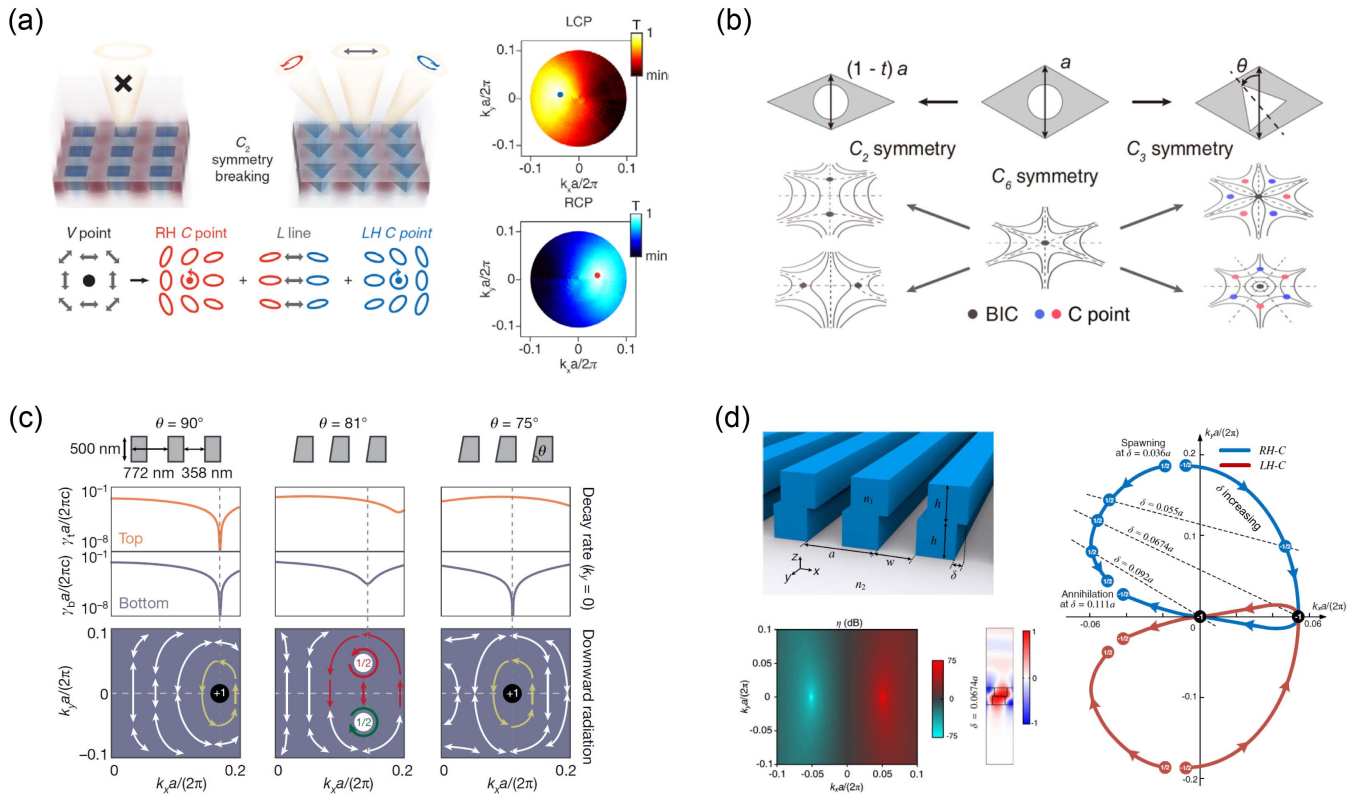
Fig. 7 Momentum-space evolution of BICs by symmetry breaking. (a) Left: schematic view of how an at-Γ BIC splits into a pair of C points. Right: experimentally measured transmittance along the band under LCP and RCP incidence[66]. L(R)CP: left (right)-handed circular polarization. (b) Schematic view of how a high-order BIC with topological charge −2 evolutes under different symmetry breaking[57]. (c) Evolution from off-Γ BIC to unidirectional guided resonance (UGR) by breaking the up-down mirror symmetry[60]. (d) Right: evolution of polarization singularities in momentum space. Left: schematic view of the 1D PhC slab constructed by two superimposed gratings and the realized UGRs[61].

Yoda *et al.*[40]. And maintaining the C_3 rotational symmetry, the rotation of C points in momentum space was also theoretically proposed and experimentally realized by Wang *et al.*[57]. These explored evolution rules of high-order BICs offer more approaches to realize the on-demand design for the off-Γ BIC and C points.

For the off-Γ BICs, it was reported by Yin *et al.* that by breaking the up-down mirror symmetry, the off-Γ BIC can also be split into a pair of C points[60]. By making the sidewall of the 1D PhC slab tilted from the vertical direction, the off-Γ BIC with topological charge +1 splits into a pair of C points with topological charges $+\frac{1}{2}$ with opposite helicities, and two C points merge to form a unidirectional guided resonance (UGR) [Fig. 7(c)]. For this achieved UGR, radiation towards the bottom is forbidden, enabled by the topological nature as the center of a polarization vortex, while the radiation towards the top remains finite. The properties are desired by many applications like energy-efficient grating couplers or antennas. By the way, it was recently reported that UGRs can also emerge from interband coupling[72], which enriches the physical generation mechanisms of UGRs. In structures without up-down mirror symmetry, the BIC and UGR can also be generated from the original region whose total topological charge is always zero[61]. By continuously tuning the misalignment δ of two superimposed identical gratings, two pairs of C points with topological charges $\pm\frac{1}{2}$

emerge in momentum space, first merging to form UGRs, then splitting and merging again to form an accidental at-Γ BIC, and finally annihilating in momentum space [Fig. 7(d)]. There is also another case for the structures without up-down mirror symmetry. When the structures' rotational symmetry is maintained, it was reported that the polarization states around at-Γ BICs can be continuously tuned from linear polarization to circular polarization by modulating twisted configurations in the unit cell of PhC slabs[73].

In these BIC-related evolution processes, the total topological charges are always conserved. The conservation of topological charges is important and can also be utilized to analyze the expected results without performing any numerical simulation.

Besides the parameters and symmetries of basic structural shapes, there are also other physical factors and symmetries that can perform modulations on BICs' evolutions. By introducing parity-time (PT)-symmetric perturbation, conventional BICs were discovered to split into a pair of PT-BICs and lasing threshold mode[74]. Modulations that can affect the refractive index of the constituent materials, such as magnetic-field-induced responses of magneto-optical materials[75], laser-induced exceptional gain[76], and phase transition of the VO_2 material[77], can also lead to similar results to those by manipulating symmetries of basic structural shapes.

3.2 Quasi-BIC

Besides the aforementioned traditional BICs that have infinite Q factors and carry topological charges in momentum space, quasi-BICs are another well-explored BIC. Quasi-BICs are resonant states observed in optical systems that exhibit properties intermediate between traditional BICs and radiative modes. For quasi-BICs, destructive interference between different waves is not perfect, allowing a weak coupling between the resonant mode and the surrounding radiation continuum. As a consequence, quasi-BICs possess a finite, yet significantly extended, lifetime compared to resonances that are strongly coupled to the continuum. High Q factors are the main attractive properties of quasi-BICs. Also, some quasi-BICs may also have vortex-related topological configurations, which are not necessary for many applications using quasi-BICs.

Understanding the generation mechanisms of quasi-BICs is pivotal in harnessing their unique attributes for an array of optical applications. Various methodologies have been devised to engineer and manipulate quasi-BICs.

The usually used method is to precisely engineer the structural symmetries. Then quasi-BICs can be obtained from original symmetry-protected BICs. By tilting the silicon pairs to break the in-plane inversion symmetry of the unit cell[25,81], high-Q quasi-BICs can be realized as a result of distortion of the original symmetry-protected at-Γ BIC [Fig. 8(a)]. As the tilted angle θ increases, the resonance-induced transmission dip gets wider, meaning decreasing Q factors. Besides, the universal formula for Q factors as a function of the generalized asymmetry parameter (quadratic dependence) is derived[25], which can also be applied to describe the Q-factor evolution law in other quasi-BIC structures via breaking in-plane inversion symmetry[66,82–84]. A similar concept of symmetry breaking can be used to design other types of quasi-BICs[85].

Recently, it was reported by Che *et al.* that quasi-BICs could also exist in quasiperiodic systems like photonic quasicrystals[53,86]. Photonic quasicrystals can have high rotational symmetry, underlying vortex polarization configurations in momentum space that are similar to symmetry-protected BICs. For quasi-BICs in photonic quasicrystal slabs, the properties of high Q factors and carrying topological charges were observed [Fig. 8(b)]. Besides photonic quasicrystal slabs, moiré structures are also explored for quasi-BICs[78,86]. For example, by twisting two graphene PhC slabs with a special angle, both the quasi-BIC and the flat band could be achieved. Such a moiré quasi-BIC was explored with a high Q factor and vortex-like far-field zero-order diffraction channel [Fig. 8(c)]. Quasi-BICs in photonic quasicrystals and moiré photonic structures enrich the varieties of photonic systems for us to design and utilize generalized BICs[87,88].

When we consider BICs in periodic structures, the outgoing waves are forbidden from the structures to free space, while the optical modes are actually extended along the transverse direction. To achieve the combination of high Q factors and in-plane trapping of light, miniaturized BICs were proposed and demonstrated by Chen *et al.*[79]. The Miniaturized BICs are constructed in the laterally combined structures [Fig. 8(d)]: a finite-sized PhC slab supporting BICs (region A) surrounded by another PhC slab with a photonic bandgap (region B). The light can be confined in the vertical direction by the original multiple BICs of region A and the transverse propagation waves are forbidden due to the photonic bandgap of region B, giving rise to

ultrahigh Q factors and small modal volumes. The concept of the miniaturized BICs can be applied in other photonic systems and applications with demand for high Q factors and three-dimensional light trapping[89–91].

Besides the Q factors, the polarization states are another important property of quasi-BICs. By symmetry-breaking perturbations, the linearly polarized quasi-BICs can be realized when the mirror symmetry is maintained. Circular polarizations, due to the importance of many applications like those in chiral optics[92], are also desired for quasi-BICs. Various designs of chiral quasi-BICs have been proposed via introducing chiral perturbations[70,71,80,93–99]. It was proposed that by constructing the unit cells with two pairs of twisted elliptical pillars [Fig. 8(e)], the leaking waves of quasi-BICs can be circularly polarized with properly chosen parameters[80]. Moreover, by modulating the perturbation parameters, i.e., the orientations of elliptical pillars, the polarization states of quasi-BICs can be expanded to the entire Poincaré sphere. It was also reported that by designing planar chiral structures[93,97], chiral quasi-BICs can be achieved. Besides constructing twisted structures and planar chiral structures, the chiral quasi-BICs were achieved by shifting C points in momentum space as well[70,71]. By breaking the in-plane inversion symmetry, the at-Γ BICs can split into pairs of C points[66], while the at-Γ quasi-BICs are usually linearly polarized due to the existence of mirror symmetry. It was proposed and experimentally demonstrated by Chen *et al.*[71] that by further introducing slant perturbations, i.e., making the etched holes slant, the C points will move in momentum space [Fig. 8(f)]. With proper slant perturbation, the C point can be shifted at Γ point, to form the chiral quasi-BIC. This method utilizes the continuous evolution of C points under slant perturbations, and can also be instructive in designing quasi-BICs with other polarization states.

The ability of quasi-BICs to persistently confine energy within the system's spectrum while maintaining some interaction with the continuum makes them a subject of ongoing research and exploration in photonics. Combined with the tunable polarization properties, quasi-BICs will offer intriguing prospects for controlling and manipulating light in optical devices and components.

3.3 Modulation on light propagation via utilizing the high Q factors of BICs

When it comes to light field manipulations, the high Q factors of generalized BICs have sparked widespread research interest, giving rise to explorations of many exotic optical phenomena. These BICs possess extraordinarily long lifetimes and extremely narrow resonance bandwidths, making them particularly well-suited for two key topics: optical field confinement and ultra-narrow linewidth control.

In the context of optical field confinement, BICs provide a means to trap and concentrate light within subwavelength-scale structures. This confinement enables the manipulation of light at scales previously unattainable. For example, BICs can be exploited to realize zero-index photonic modes[100–104]. It was proposed by Huang *et al.* that the zero-index effect can be realized in two-dimensional photonic crystals of which the dispersion is Dirac-like in the vicinity of the Γ point[100]. However, for the practical three-dimensional cases like PhC slabs, the intrinsic loss due to radiation will usually cause a very large propagation loss[105], and the additional metal mirror to avoid radiation would
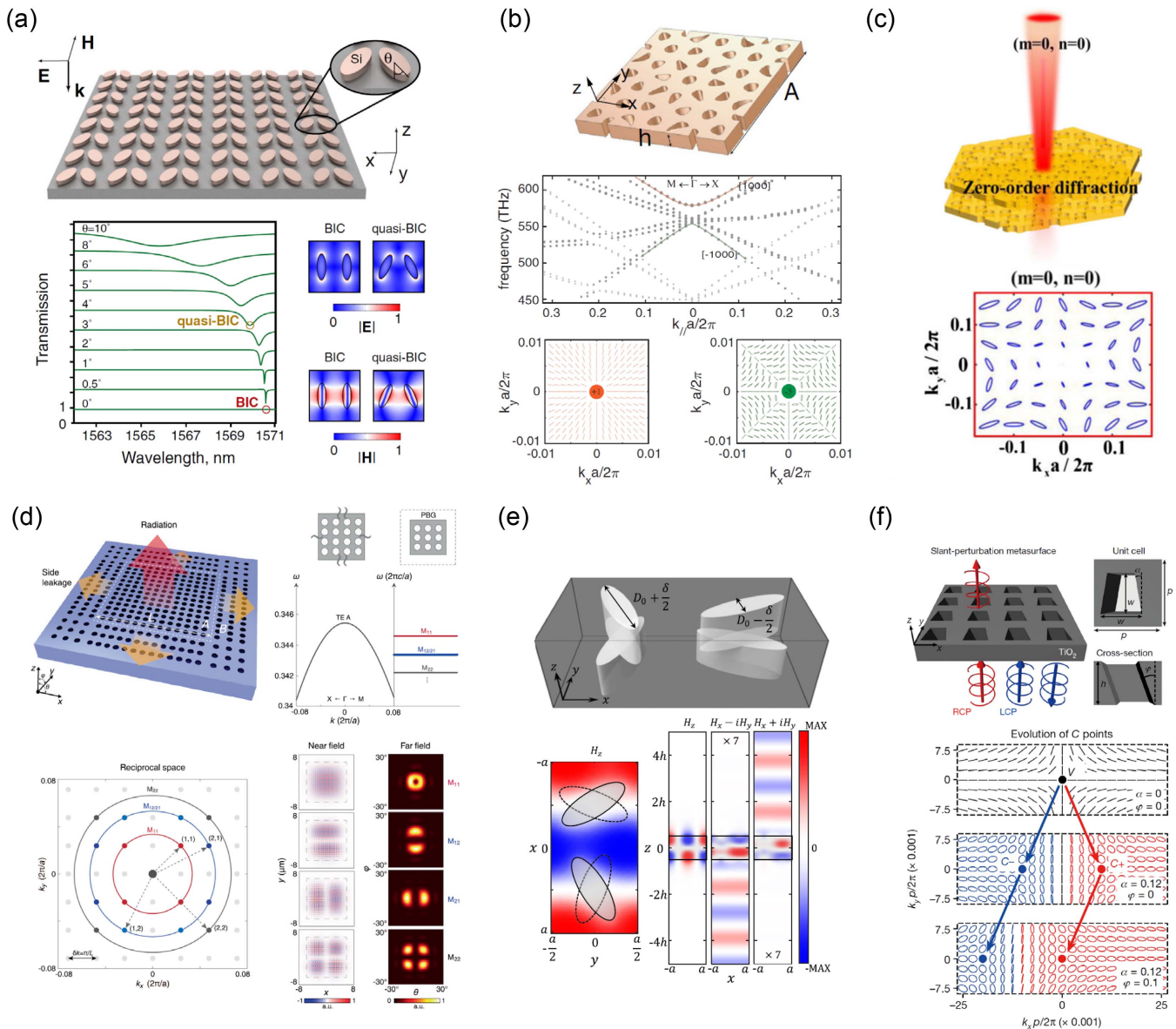
Fig. 8 Various types of quasi-BICs. (a) Quasi-BICs realized by tilted silicon-bar pairs[25]. The Q factor can be modulated by the symmetry-breaking factor. (b) Quasi-BICs in photonic quasicrystals[53]. Unfolded dispersions and polarization maps show this quasi-BIC can also carry polarization vortices in momentum space. (c) Quasi-BIC in a moiré structure composed of twisted bilayer graphene PhC slabs[78]. The vortex configuration can be found in the zero-order diffraction. (d) Miniaturized BICs constructed by laterally combined structures[79]. The miniaturized BICs can confine the in-plane light field by adding a surrounding PhC slab with an overlapped photonic bandgap. (e) Chiral quasi-BIC in perturbed structures, whose unit cells are composed of two pairs of twisted elliptical pillars[80]. The magnetic field distributions show that the chiral quasi-BIC leaks to circularly polarized light. (f) Chiral quasi-BIC in a slant-perturbation structure composed of a square array of slanted trapezoid nanoholes[71]. The momentum-space polarization distributions of different slant perturbations exhibit the generation process of this chiral quasi-BIC.

give rise to absorption loss[101]. To avoid those problems, symmetry-protected BICs at Γ point are proposed to realize zero-index modes without radiative loss[102]. In the PhC slabs with a designed Dirac cone at Γ point, in which the zero-index modes are also BICs, the low-loss zero-index propagation of light can be realized in an all-dielectric photonics platform [Fig. 9(a)]. Besides the zero-index effect, the properties of trapping light

by BICs can also lead to the realization of three-dimensional cases, which are usually discussed in two-dimensional space. By utilizing off-Γ BICs, the on-chip negative refraction was also reported[106] [Fig. 9(b)]. Recently, BICs have been found to be able to realize enhancement of evanescent field localization[107].

When light shines on structures from free space, the high Q factor of BICs can lead to another effect of light confinement:
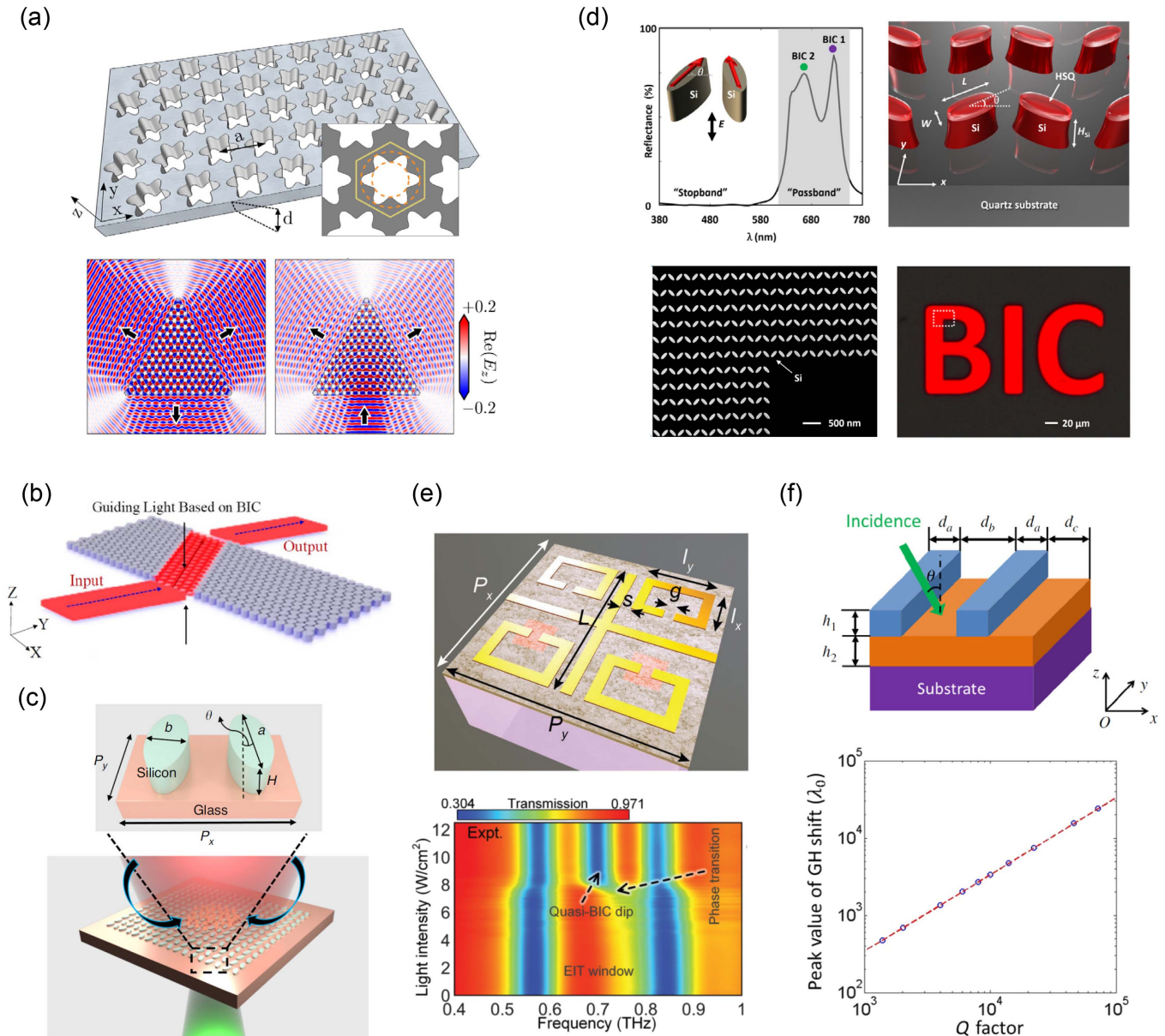
Fig. 9 Modulating the flow of light via the high Q factors of BICs. (a) Zero-index propagation effect enabled by symmetry-protected BICs in a C_{6v} PhC slab[102]. (b) Negative refraction mediated by BICs[106]. (c) Optofluidic transport and assembly of nanoparticles by utilizing strong electromagnetic field enhancement of the quasi-BIC resonance[111]. (d) Saturated reds by quasi-BICs[112]. (e) Steering spatiotemporal spectra by actively tailoring BICs[77]. (f) Giant enhancement Goos-Hänchen shift by quasi-BICs[113].

strong near-field enhancement. When light waves pass through the photonic structures, the excited resonances of quasi-BICs will strongly enhance the near field around the structures, giving rise to many applications for further modulation by light. The enhanced optical forces by the confinement of light were reported and applied to trap nanoparticles[108–110]. The near-field enhancement of quasi-BICs will also cause a localized heating effect, which was reported to realize optofluidic transport and assembly of nanoparticles[111] [Fig. 9(c)].

Moreover, the ultra-narrow linewidth control afforded by high-Q BICs holds significant promise for precise spectral engineering and filtering effects. The Huygens's condition and

BICs were bridged to realize extreme Huygens' metasurfaces with high Q factors[114]. Saturated reds were reported by utilizing quasi-BICs[112]. By specially designed Si nanoantennas, sharp reflectance spectra at red wavelengths can be obtained by partially overlapping resonances of two quasi-BICs, and the reflectance at blue/green wavelengths can be suppressed by the substrate-induced diffraction and the absorption of amorphous Si [Fig. 9(d)]. With the ultra-narrowband filtering abilities, quasi-BICs can be further applied to design the integrated spectrometers[115]. Combined with phase transition materials like VO₂, the dynamic tuning of transient photoconductivity can be utilized to induce spatial symmetry breaking, hence actively

multidimensional lineshape tailoring can be achieved by modulating BIC-mediated photon cavities[77] [Fig. 9(e)].

Besides the direct spectral modulation, high Q factors of BICs can realize the spatial modulation of light beams, such as the well-known Goos-Hänchen (G-H) shift[116]. G-H shifts are closely associated with the momentum-space phase gradients[113,117–119]. The high Q factor of quasi-BICs would lead to sharp incident-angle-dependent reflection or transmission, giving rise to drastic changes in the resonant phase in momentum space. Hence, enhancement of G-H shifts is expected. For instance, it was reported by Wu *et al.* that by utilizing quasi-BICs of a compound grating waveguide structure, the giant enhancement of G-H shifts could be achieved together with high reflectance[113] [Fig. 9(f)]. With a coupled double-layer grating, the method to realize large G-H shifts with high transmittance was also proposed[120].

3.4 Light manipulations via utilizing the topological nature of BICs

Surrounding BICs, the major axes of polarization state wind in the clockwise or anticlockwise direction. This winding topological nature of BICs has been explored with many topological effects, bringing new degrees of freedom to manipulate light.

The vortex configurations around BICs are naturally connected with the vortex-like resonant responses, showing potential to modulate optical vortices. It was reported by Wang *et al.* that a momentum-space polarization vortex can be leveraged to induce wave-vector-dependent Pancharatnam–Berry (PB) phases; then the optical vortex can be generated using the momentum-space approach[121]. Considering the simple case in which a plane wave shines on the PhC slab, the transmission or reflection process can be described by

$$|E_{\text{out}}\rangle = \begin{bmatrix} s_{ll} & s_{lr}e^{2i\theta(\mathbf{k}_\parallel)} \\ s_{rl}e^{-2i\theta(\mathbf{k}_\parallel)} & s_{rr} \end{bmatrix}|E_{\text{in}}\rangle \qquad (6)$$

on a helical basis, where s refers to the transmission or reflection coefficients and the subscripts $l(r)$ correspond to the LCP and RCP. Here, the θ is the azimuthal angle of the eigen-polarization at the wave vector $\mathbf{k}_\parallel$. It can be seen that in off-diagonal elements there are additional geometric phase factors, i.e., PB phases, related to θ. For example, when a circularly polarized light beam shines on the PhC slab, the cross-polarized transmitted light beam will gain a spiral phase front due to obtained winding PB phases surrounding BICs [Fig. 10(a)]. Note that the PB phases are loaded in momentum space, exhibiting a new principle to generating an optical vortex. For this optical vortex generator based on BICs, the center alignment is not required because the PhC slabs are actually periodic structures in real space. To pave the road for further applications, the effective methods to improve the generating efficiency of the BIC-based method are proposed and experimentally demonstrated[122,123]. Besides the linear optics, the optical vortex generation based on BICs is also proposed in the nonlinear conversion[124]. The transformation of the polarization vortex in momentum space to the winding phase of light beams exhibits a new form of spin–orbit interactions (SOIs) in photonic crystals[125]; more SOI-related phenomena are expected in the momentum-space topology of BICs.

The SOIs of light would lead to some representative phenomena, including spin-to-vortex conversion and the spin-Hall effect

of light[129]. The vortex generation has shown the overall effect of topological vortex configurations of BICs to realize spin to vortex conversion[121–123]. Focusing on a local part of the topological polarization vortices around BICs, one case of the spin Hall effect of light, i.e., spin-dependent beam shift, has also been revealed[126]. The beam shifts can be generally summarized as the momentum-space phase gradients[119], i.e.,

$$\langle \mathbf{R} \rangle = \mathbf{R}_0 - \left\langle \frac{\partial \phi(\mathbf{k}_\parallel)}{\partial \mathbf{k}_\parallel} \right\rangle, \qquad (7)$$

where $\mathbf{R}_0$ is a ϕ-independent constant. From this perspective, the spin-dependent beam shifts are expected in topological vortices around BICs. Besides the PB phases due to the winding polarization states, the nonlocal resonance between the incident light and optical modes in PhC slabs will induce an additional resonant phase. Combined with both PB phase gradients and nonlocal resonant phase gradients in momentum space, a new type of spin-dependent beam shift was proposed and experimentally demonstrated in PhC slabs via topological vortices around BICs. When a circularly polarized light beam shines onto the PhC slab, the cross-polarized converted reflection light beam will have a spin-dependent in-plane-oblique shift relative to the incident light beam [Fig. 10(b)]. With a similar beam shift principle based on momentum-space phase modulation, the beam shifts at normal incidence were also realized by utilizing pairs of topological half vortices split from BICs[66,119]. These momentum-space topological polarization vortices offer new polarization degrees of freedom to modulate beam shifts, and can also inspire on-chip applications for spin optics.

The winding polarization states around BICs enable the existence of various resonant coupling coefficients; hence structures with BICs can serve as good platforms for polarization control. In reflection-type structures, complete polarization conversions can be realized[130–132], in which the BICs are found to lie on the critical coupling curve that defines a complete polarization conversion condition[130]. For fixed incident polarization, the output polarization state can be manipulated by changing the incident angle. Moreover, in structures enabling both reflection and transmission, by utilizing multiple inputs with controlled relative phases, the achievement of coherent complete polarization conversion near the symmetry-protected BIC was also proposed[127]. The radiative coupling variation due to the strong polarization transition around BICs and the phase control of two input beams are combined together to perform feasible polarization control [Fig. 10(c)]. By this means, full polarization control on the entire Poincaré sphere can be realized by structures supporting a symmetry-protected BIC. These scattering behaviors embodied in the topological features of BICs can inspire novel optical elements for polarization control.

What is more, it was reported by Qin *et al.* that topological features of optical force distribution exist in momentum space[128]. The topology of optical force distribution is associated with the topological polarization configurations around BICs. By using twisted PhC slabs, various topological configurations of optical force distribution can emerge along with the variation of the eigen-polarization distribution [Fig. 10(d)]. Combined with the aforementioned properties of polarization control and structural optical field generations by utilizing the topological configurations around BICs, there are still many topological effects in optical forces to be further explored.
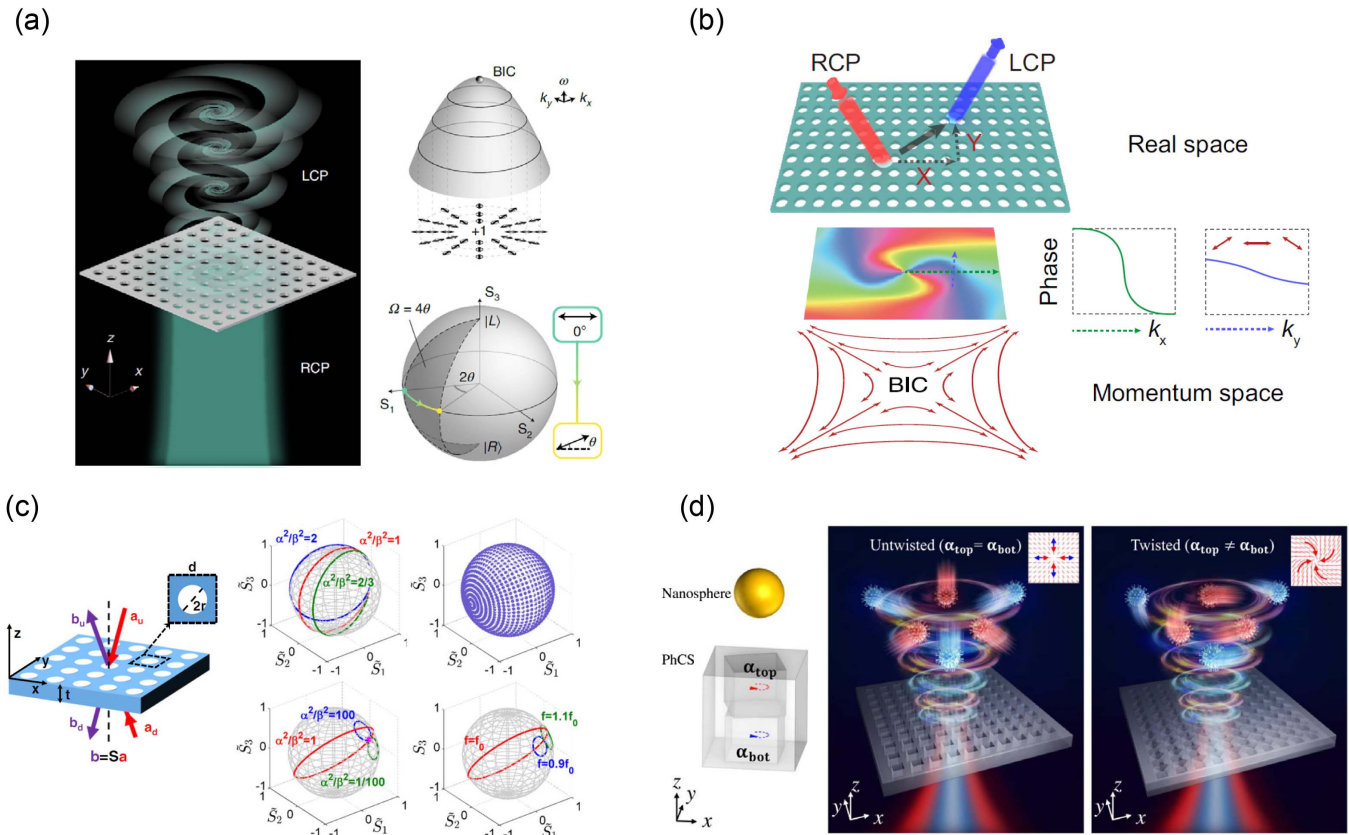
Fig. 10 Manipulating light by utilizing the topological vortex configurations around BICs. (a) Generating optical vortices via momentum-space polarization vortices around BICs[121]. LCP and RCP denote the left- and right-handed circularly polarized lights. When an RCP Gaussian beam shines normally on the PhC slab, the converted LCP light beam will obtain a spiral phase wavefront via resonant responses with the polarization vortex around the BIC. (b) Spin Hall shifts of light via momentum-space polarization vortices around BICs[126]. When a circularly polarized light beam obliquely shines on the PhC slab, the cross-polarized light beam will have a spin-dependent lateral light beam shift due to the momentum-space phase gradients enabled by polarization vortex around the BIC. (c) Polarization control around BICs with two phase-controlled inputs[127]; a and b correspond to two input waves. In the presence of multiple input beams, the topological features of BICs enable full polarization control on the entire Poincaré sphere. (d) Topological features of optical force distribution around BICs[128]. In contrast with untwisted PhC slabs, twisted PhC slabs can trap nanoparticles with a spinning pattern.

3.5 Light–matter interactions

3.5.1 Strong coupling

Cavity quantum electrodynamics (CQED) mainly focuses on the interaction between quantized fields and quantum emitters in limited space, like microcavities[133–136]. When the energy exchanging strength between quantum emitters and cavity modes is much larger than the loss rates of photons and excitons, CQED systems enter the strong coupling regime in which a quasi-particle named polariton appears with both photonic and excitonic components[137]. Rabi splitting caused by strong coupling can be explained by the dressed state theory[138] and observed in the spectrum[134,135,139]. For planar photonic structures, distributed Bragg reflectors (DBRs) are often used as a cavity in the vertical dimension[140–144]. However, nowadays, the BIC can enhance the strong photon-exciton coupling instead of DBR mirrors because BIC cavities provide higher Q factor and

near-infinite photon lifetime[16,22,145]. Therefore photonic CQED systems can more easily achieve strong coupling and obtain large Rabi splitting, leading to strong implications for polaritons in quantum information processing[146,147].

Most research combining BICs and strong coupling is based on hybrid planar photonic structures comprising BIC PhC slabs and excitonic layers like quantum wells (QWs)[137,140] or quantum dots (QDs)[150]. To achieve strong coupling at room temperature, transition metal dichalcogenides (TMDCs) like WS_2 or WSe_2 are often utilized to couple monolayer excitons to a topologically protected BIC. Figure 11(a) shows a typical BIC-strong coupling research with TMDC materials by Maggiolini *et al*[148]. The PMMA grating is fabricated on the top of a DBR-WS_2-SiO_2 structure with a defective subwavelength structure, showing strong light–matter interaction enhancement and large exciton-polariton nonlinearities at room temperature. Then a Rabi splitting of 70 meV is achieved by a structured
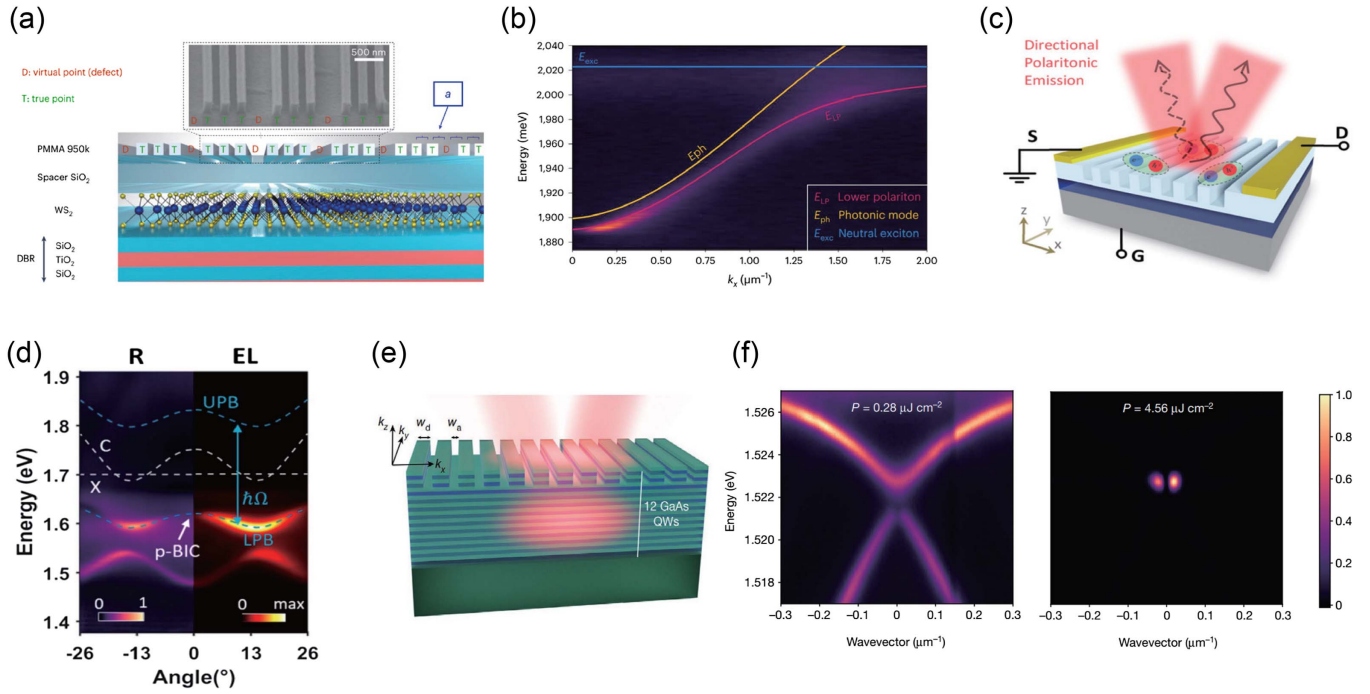
Fig. 11 Researches of photonic BIC combined with strong coupling and photonic BEC. (a) Sketch of the BIC-strong coupling system with a PMMA grating fabricated on the top of a DBR-WS$_2$-SiO$_2$ structure[148]. (b) Fitting of the PL dispersion at the anticrossing leading to a 70 meV Rabi splitting by (a)'s structure[148]. (c) Schematic of the electrically driven perovskite metasurface with tunable polaritonic emission leading to strong coupling of photonic modes and electrically injected excitons[149]. (d) Experimental angle-dependent reflection spectra of the active perovskite metasurface under TE illumination, showing the Rabi splitting[149]. (e) Sketch of the polariton waveguide with partially etched 1D lattice combining BIC and polariton BEC[147](f) Left panel: angle-resolved photoluminescence emission showing the dark spot on the lower polaritonbranch from the BIC. Right panel: on increasing the pumping power, the measured polariton dispersionshows a two-lobe emission, which is the characteristic of polariton BEC[147].

optimization approach [Fig. 11(b)], paving the way to topologically protected polariton devices. Besides using the TMDC monolayer over or inside the periodic structures[151–156], fabricating bulk TMDC materials to form metasurfaces can efficiently improve the spatial overlap of the cavity mode profile with the emitters to make more significant strength of light–matter interaction. While several theoretical bulk WS$_2$ works give large Rabi splitting that even exceeds 200 meV[157–161], recent experiments show a tuned strong coupling system with maximum Rabi splitting of 116 meV by constructing BIC-driven metasurfaces composed of bulk WS$_2$[162]. Besides TMDC materials, perovskite metasurfaces are also worth trying to enhance the strength of light–matter interaction. As shown in Fig. 11(c), Y. Wang *et al.* performed an electrically driven perovskite metasurface with tunable polaritonic emission[149]. This can achieve strong coupling between injected excitons and photonic BIC of a one-dimensional perovskite metasurface. They observed the formation of high-Q BICs leading to a large Rabi splitting of ∼200 meV [Fig. 11(d)]. By carefully designing the perovskite-based metasurfaces, it is possible to increase the Rabi splitting to over 200 meV[163,164]. Moreover, without special emitters like TMDCs or perovskites, the strong coupling can still be reached by carefully designing BIC photonic plasmonic/dielectric structures[32,165–171].

When strong coupling systems follow the criteria for condensation,

$$T_{\text{crit}} = \left(\frac{\nu}{2.612}\right)^{2/3} \frac{h^2}{2\pi m k_B},\qquad(8)$$

where T_{crit} is the critical temperature, ν is the particle density, m is the particle mass, and k_B is the Boltzmann constant. The whole polariton gas in the condensed state will be described as a single giant matter wave and obey Bose-Einstein statistics, which is called Bose-Einstein condensation (BEC). Especially owing to the little effective mass, larger particle density, and higher critical temperature, polaritons in QW microcavities offer an excellent testbed for BEC and even for the new coherent light source called the polariton laser[172,173]. Distinguished from cold atom BEC, the polariton BEC requires to be continuously repopulated to compensate for optical losses via optical pumping or electrical current injection[174–178]. Ardizzone *et al.* first showed polariton BEC occurring in a BIC using a patterned waveguide[147]. As shown in Fig. 11(e), they fabricated a GaAs QW with 12 periods and etched a one-dimensional BIC-PhC structure with a lattice constant of 243 nm and a groove deep of 90 nm. Here multilayer QW with N periods not only enhances strong coupling strength with $\sqrt{N}$ times[133,134,143] but also

keeps the polariton density in QWs under the Mott density[179,180]; otherwise, the system naturally enters a weak coupling regime. The etched BIC-PhC pattern makes QWs function as both emitters and photonic cavities. It improves the spatial overlap of the cavity mode profile with emitters, which benefits the formation of polariton BEC. As shown in the left panel of Fig. 11(f), under non-resonant excitation, the photoluminescence spectra show a dark spot on the lower polariton branch from BIC. On increasing the pumping power, the measured polariton dispersion shows a two-lobe emission, which is the characteristic of polariton BEC [the right panel of Fig. 11(f)]. With the increment of the energy density of the input pump, the polariton presents three regimes divided by two thresholds: polariton LED, polariton laser, and photonic laser. In the polariton LED regime, particles obey Boltzmann distribution without coherence. When crossing the first threshold, the system enters the strong coupling regime, polaritons condensate, and polariton lasing appears. This regime is also called polariton BEC or polariton laser regime. Note that a polariton laser is caused by stimulated scattering of polaritons, not stimulated emission of photons, which differs from a photonic laser[172]. Near the first threshold, several phenomena are unitized to judge whether the BEC phase transition happens. First, the observed phase transition comes with the narrowing of the condensate linewidth in both real space and momentum space[174,181,182]. Second, polariton-polariton interaction causes a blueshift of the polariton emission around the condensation threshold[176,183]. Thirdly, spatial coherence and visibility of interference fringe can be measured above the first threshold owing to the finite expansion of the long-range order within the condensate area[147,184]. Finally, the bunching effect of $g^{(2)}$ can also mark the first threshold by Hanbury-Brown-and-Twiss (HBT) measurements[185]. When the input crosses the second threshold, the particle density exceeds the Mott limit; thus, the strong coupling regime turns to a weak coupling regime. The polaritons lose the matter components and turn to pure photons, leading to the coherent photonic laser. Polariton and photonic lasers are both coherent lights, so it is more challenging to distinguish them. The measurement of Zeeman splitting could be a way that needs large external fields[181]. For now, many kinds of materials are suitable for microcavities to study polariton BEC, like III/V[186] and II/VI[187] materials for low temperature, or GaN[188], ZnO[189], organic materials[142], perovskites[190], and TMDCs[191] for room temperature. Since the first study of BEC from BIC based on GaAs proposed by Ardizzone *et al.*[147], one has also explored the BIC-based BEC by other materials, like perovskites[184] and organic perylene dyes[192], with similar results.

3.5.2 Nonlinear enhancement

Owing to the radiation suppression abilities and large fabrication tolerance under topological protection, light confinement with ultra-high Q factors and small modal volume Vs can be achieved with BICs. The BIC structures then show great potential in optical nonlinearity enhancement under a large Purcell effect described by Q/V. In 2018, Carletti *et al.*[193] made a prediction about the enhancement of second harmonic generation (SHG) in an AlGaAs nano-antenna supporting BIC states. The efficiency could be two orders of magnitude stronger than that in conventional designs. In 2020, from the same research group, Koshelev *et al.*[194] experimentally implemented a design with a quasi-BIC mode realized by the mutual interference of several

Mie modes, as illustrated in Fig. 12. The quasi-BIC state with a Q factor of 188 was observed in the particle with a diameter of 930 nm and height of 635 nm. Two orders of magnitude higher conversion efficiency was achieved as expected.

The nonlinearity of higher orders has also been explored. In 2019, Xu *et al.*[198] demonstrated a silicon metasurface and observed a third-harmonic generation (THG) with a conversion efficiency of 5×10^6 at 100 mW. In the same year, Liu *et al.*[82] realized a record-high Q factor of 18511 also in a silicon metasurface, and observed a THG conversion efficiency five orders of magnitude higher than the former silicon metasurfaces. The field enhancement was large and even the SHG in silicon was also observed. Moreover, Kang *et al.*[199] demonstrated the third- and fifth-harmonic optical vortex generation numerically from an amorphous silicon photonic crystal slab.

Among these works, various methods were considered to enhance the nonlinear transform efficiencies. On one hand, the doubly resonant design, where both the excitation and its harmonics were supported resonances in the structure, would help to maximize the efficiency. Wang *et al.*[195] realized a doubly resonant GaN photonic cavity in which the fundamental frequency matched with a defect mode and its second-harmonics operated upon a quasi-BIC. The final intrinsic conversion efficiency got 10 times larger than singly resonant cavities in GaN. On the other hand, the field strength can be further enhanced considering the coupling conditions. Xu *et al.*[198] and Koshelev *et al.*[200] constructed critical-coupling conditions by slightly breaking the in-plane symmetry that shifted the resonance away from the complete dark BIC.

The great enhancement of nonlinear effects leads to applications in frontier domains such as quantum optics. In 2022, Santiago-Cruz *et al.* generated entangled photons via spontaneous parametric downconversion in GaAs metasurfaces supporting a quasi-BIC state. A single resonance or several resonances pumped at multiple wavelengths could also generate multifrequency quantum states, including cluster states.

Besides the conventional dielectric nonlinear materials, 2D thin-film materials were also attractive in the nonlinear effects of evolving BIC states. In 2020, Kravtsov *et al.*[152] demonstrated a BIC-based polaritonic excitation with MoSe$_2$ upon PhCs, in which strong exciton-fraction-dependent optical nonlinearities were exhibited. In 2021, Liu *et al.* demonstrated a giant second-harmonic generation (SHG) enhancement with silicon metasurfaces supporting quasi-BICs covered by 2D GaSe flakes. The SHG from a GaSe flake is uniformly enhanced by nearly four orders of magnitude with the field enhancement.

4 Applications

4.1 BICs in lasing

Given the BICs' innate ability to realize high-Q resonances, the most significant application of BICs is for lasing. Photonic crystal surface-emitting lasers (PCSELs)[201] with periodically arranged photonic crystal structures are one kind of novel semiconductor laser. Although not specifically mentioned, in the most common case in which the periodic lattice and unit cells of PCSELs respect C_2 or higher in-plane symmetry, the lasing band edge modes operating at the second-order Γ point are actually the symmetry-protected BICs[202,203], which supports large area coherent oscillations. In the past two decades, PCSELs have attracted considerable attention as the successor of DFB lasers and experienced dramatic developments that surpass
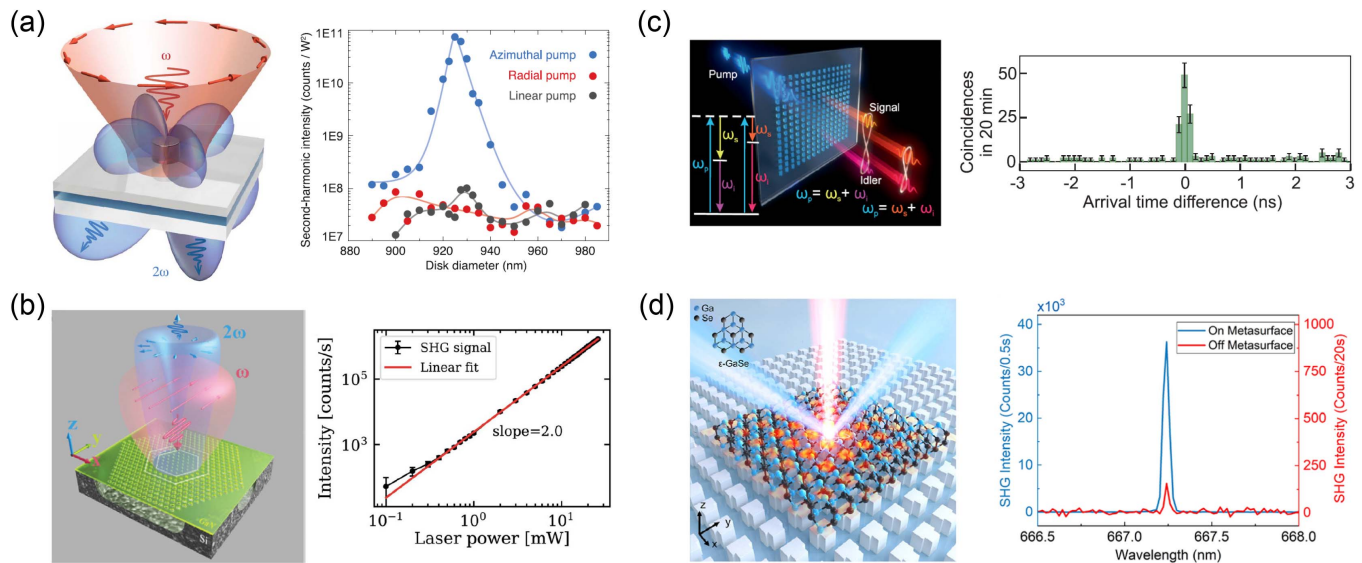
Fig. 12 Light–matter interaction enhancement and nonlinear optics. (a) Diagram of second harmonic generation (SHG) in a metal antenna (left), and the measured SH intensity versus nanoresonator diameter at different pump polarizations (right). The SH intensity is normalized on the square of the pump power[194]. (b) Diagram of enhanced SHG in a doubly resonant cavity (left) and the measured SHG intensity (right). The red and blue lobes represent the far-field intensities of the first-harmonic (FH) and SH modes, respectively[195]. (c) Conceptual diagram (left) and typical distribution of the photon arrival time difference for two detectors (right), of multiplexed entangled photon generation by spontaneous parametric downconversion utilizing BIC in a metasurface. The photon arrival time difference demonstrates photon pair generation[196]. (d) Conceptual diagram (left) and measured SHG intensity (right) of an enhanced SHG with a 2D GaSe flake on a metasurface with a BIC state[197]. The GaSe flake was laid on the surface of a Si metasurface consisting of a periodic square lattice of T-shaped pillars.

traditional semiconductor lasers. The evolution of PCSELs has been covered in detail in other reviews[204], with a few of the key events listed as follows: the first lasing action of PCSELs was reported in 1999[201] [shown in Fig. 13(a)]; current-injected lasing under room-temperature and continuous-wave operation was achieved in 2004[205]. Over the next few years, PCSELs' capabilities were expanded, including tailoring the beam patterns in 2006[206], extending the lasing wavelength to the blue-violet region in 2008[207], and achieving beam-steering functionality in 2010[202]. Increasing the output power of lasers is a long-term topic; through continuous optimization of structural design, watt-class lasing was realized in 2014[208] followed by 10-watt-class lasing in 2019[209] and lasing with a peak power of 20 W in 2021[210]. Recently, on-chip beam scanning lasers were first achieved[211] as illustrated in Fig. 13(b), and lasing with a CW output power exceeding 50 W, purely single-mode oscillation and a narrow beam divergence of 0.05° was reported[212]. It is worth mentioning that in the early years, PhCs in PCSELs were mainly composed of circular hole structures, so the lasing modes were theoretically the symmetry-protected BICs with infinite Q factors. In high-power lasers, the in-plane C_2 symmetries were broken for higher-efficiency power extraction, leading to the generation of quasi-BICs with high but finite Q values[208,209,212].

Lasing from BICs has also been developed in other materials with periodic structures in addition to PCSELs. In 2017, Kodigala *et al.*[215] demonstrated the optical-pumped single-mode lasing from the cavity made of an array of suspended In$_x$Ga$_{1-x}$As$_y$P$_{1-y}$ multiple-quantum-well cylindrical nanoresonators. In 2018, using vertical electric dipole resonances excited inside GaAs nanopillars to form BICs, Ha *et al.*[213] reported directional lasing in arrays of active dielectric nanoantennas, as illustrated in Fig. 13(c). In 2022, Contractor *et al.*[216] demonstrated Berkeley surface-emitting lasers (BerkSELs) based on open-Dirac singularities. They are robust against size scaling and single-mode lasing is maintained even for near-damage-threshold pump power. What is more, lasing action has also been reported in Mie-resonant BICs. In 2020, Wu *et al.*[217] reported optically pumped room-temperature lasing in a solution-processed CdSe/CdZnS nanoplatelet film with an all-dielectric cavity supporting BICs, which arise from Mie resonances in square-latticed TiO$_2$ nanocylinders.

Besides symmetry-protected BICs, other types of BICs including super-BICs and mini-BICs have also been adopted to increase cavity Q factors and lower the lasing threshold. In 2021, Hwang *et al.*[214] reported lasing action from super-BICs based on a finite-sized PhC cavity, as illustrated in Fig. 13(e). Originating from the merging of several BICs in the momentum space, the radiation loss in super-BICs follows the law k^6 depending on the lattice constant and the super-BICs keep a high Q factor even in the finite-sized cavity, thus reducing the lasing threshold to a large extent. On the other hand, Ren *et al.*[90] demonstrated active mini-BIC lasers with Q factors as high as 32,500 in 2022 [shown in Fig. 13(d)], which had a record-low threshold of 80 W/cm^2 that was nearly two orders of magnitude lower than other BIC lasers. The laser cavity is based on PhCs
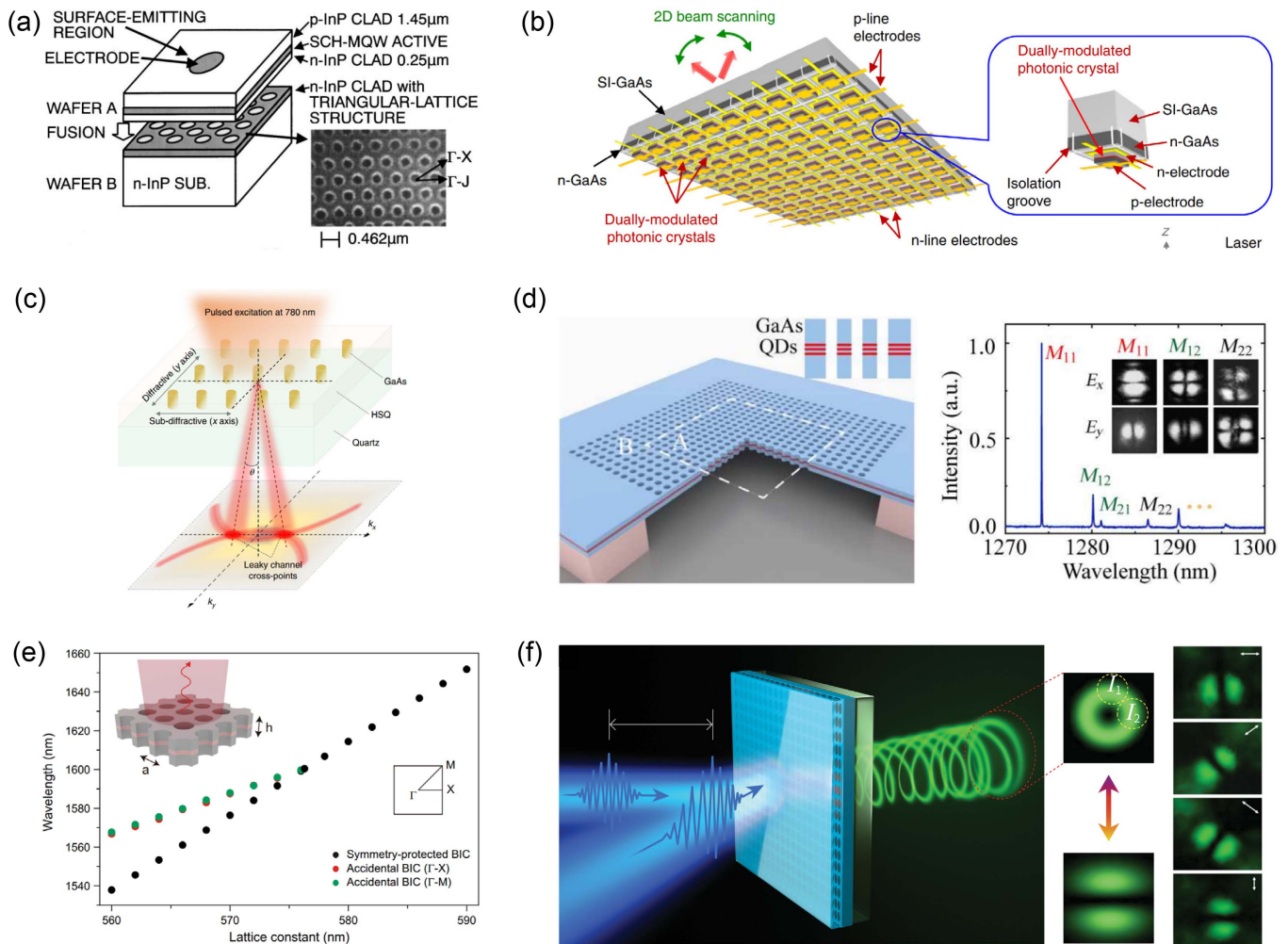
Fig. 13 Applications of BIC in lasers. (a) Schematic structure of the first lasing PCSEL based on the wafer fusion technique. The inset shows the SEM photograph of the triangular-lattice structure[201]. (b) Dually modulated on-chip beam scanning lasers. Each unit can be selectively operated by driving the corresponding line electrodes[211]. (c) Directional lasing in resonant GaAs nanopillar array[213]. (d) Left: schematic of mini-BIC laser device consisting of a suspended GaAs thin membrane with periodically etched airholes. Right: microphotoluminescence (μ-PL) spectrum of the cavity modes[90]. (e) Merging of the BICs in super-BIC laser[214]. (f) All-optical switching from the vortex microlaser. Insets show the far-field emission patterns at different pumping densities[76].

consisting of a suspended GaAs membrane with InAs QDs embedded in the center, in which the out-of-plane radiation is suppressed by BICs and the in-plane light confinement is achieved by PBGs through fine horizontal hetero-structural design. In 2023, Zhong *et al.*[91] reduced the lasing threshold of mini-BIC lasers to 52 W/cm² by enabling effective trapping of both light and carriers in all three dimensions.

Through tuning the topological charges, BICs can be utilized to realize varied beam patterns as well. Early attempts include experiments on the generation of tailored beams in PCSELs[206]. Recently, because it has great potential in upgrading optical communication systems to higher multiplexing levels, vortex beam and chiral beam generation has attracted much attention. In 2020, Huang *et al.*[76] reported perovskite-based vortex lasers and their applications to all-optical switching, as shown in Fig. 13(f). The BIC resides at the Γ point and exhibits a vortex. Through modifying the two-beam-pumping configuration,

ultra-fast switching between a vortex beam and a regular linearly polarized beam was realized with a transition time of only 1.5 ps. In 2022, Zhang *et al.*[70] demonstrated chiral emission from resonant metasurfaces that were created by a square lattice of tilted TiO_2 bars placed on an ITO-coated substrate. By breaking in-plane and out-of-plane C_2 symmetries, intrinsic chiral quasi-BIC appears at the Γ-point. While pumping above the threshold, the intensity of the LCP mode dominates the emission spectrum, resulting in single-mode lasing operation. In addition to the above mentioned, chiral emission was also realized in spin-optical light sources including the spin-valley Rashba monolayer laser[218] and the spin-valley-locked perovskite laser[219].

4.2 BICs in sensing

Structures incorporating BICs inherently exhibit high-Q resonance behavior, with the ideal scenario being an infinite
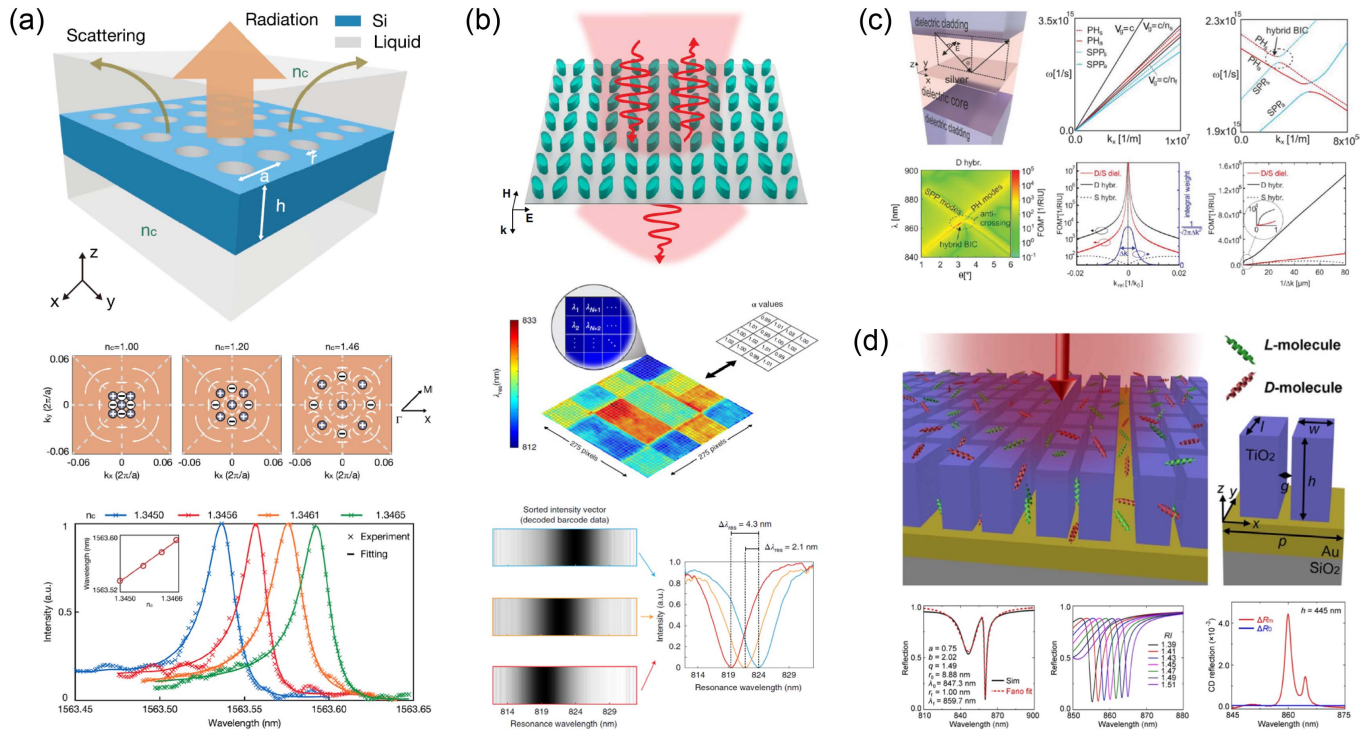
Fig. 14 Applications of BIC in sensors. (a) Topological charge evolution and refractive index sensing of merging BICs based on a BIC PhC slab[246]. (b) Hyperspectral imaging and biodetection enabled by BIC metasurfaces[253]. (c) Hybrid BICs-enhanced senor with a plasmonic component enables strong field confinement[254]. (d) Chiral layer-enhanced sensing applications enabled by BIC metasurfaces[241].

Q factor. In a disturbed environment, the ideal BIC transforms into a quasi-BIC with an offset resonant wavelength while maintaining a fairly high Q factor. This unique property renders it highly applicable in various optical and photonic contexts[220–228]. Given the distinctive characteristics of topological polarization singularities within radiation fields, their utilization in sensing appears logical. The promising attributes of high-Q-integer charges (BICs) and the chiral responses of half-charges (CPs) offer considerable potential. The realm of high-Q resonators has realized high-sensitivity refractive index (RI) sensing across chemical and biological processes, as evidenced by various studies[229–239]. Remarkably, RI sensors exploiting BICs, as manifested in dielectric metasurfaces[238–242], plasmonic metasurfaces[123,243,244], and PhC slabs[227,245,246] have exhibited promising advancements in terms of figure-of-merit (FOM) and detection limit (DL). Concurrently, metasurfaces supporting quasi-BICs can demonstrate even better performance by providing giant chiroptical signals because of their higher Q factor, which has led to significant progress in chiral sensing[199,247,248]. Furthermore, it is worth noting a novel category of methodologies that indirectly leverage exceptional points (EPs) to enhance sensing performance, influenced by their underlying connections to polarization singularities[249–252].

Localized PhC defect cavity[231,237] sensitivities are restricted due to limited field overlap with the analyte. Slotted PhC cavities[255,256] offer higher sensitivity by enhancing the mode field overlap with the analyte. However, they are susceptible to fabrication imperfections. Using BICs in PhC slabs for sensing, as opposed to traditional defect-based PhC slabs sensors, offers

benefits like reduced radiation loss and enhanced light-analyte interactions. To enhance sensing performance, addressing out-of-plane scattering loss due to fabrication imperfections is crucial for improving Q factors. Lv *et al.*[246] employed a merged BIC design in RI sensing, significantly enhancing detection limits up to 10^{-5} RIU through increased Q values [Fig. 14(a)]. This underscores the promise of this sensor design for applications including biochemical sensing, environmental monitoring, and medical diagnostics. Additionally, the sensitivity of RI sensors depends on aligning optical resonances with target substances in the surrounding environment.

Metasurfaces offer a versatile solution to this challenge. Techniques like breaking in-plane symmetry or utilizing low-contrast materials have been developed on platforms such as PhC slabs[257] and dielectric metasurfaces[238,239,258], with broad applications. By mapping absorption signatures of molecules onto spectra formed by quasi-BICs, where each quasi-BIC corresponds linearly to pixel locations, molecular barcoding offers heightened sensitivity for detecting molecular fingerprints[81]. As a result, the current trend to combine hyperspectral imaging with data science techniques has led to quasi-BIC dielectric metasurfaces, serving as an ultra-sensitive, label-free sensing platform without the need for spectrometers[238,239]. Integrating pixelated BIC metasurfaces with a commercial complementary metal oxide semiconductor camera allows the detection of fewer than 3 molecules$/\mu m^{2}$[253] [Fig. 14(b)]. Commonly, plasmonic sensors encounter an inherent problem of absorption loss when compared to quasi-BIC sensors utilizing dielectric nanostructures[259,260]. However, recent findings suggest that hybrid

BICs exhibit robust field confinement attributed to their plasmonic component, leading to a tenfold sensitivity improvement over pure dielectric BICs[254] as shown in Fig. 14(c). This suggests that hybrid BICs have the potential to outperform fully dielectric systems in sensing applications and are well-suited for accommodating higher integration densities.

On the other hand, chiral sensing is essential in medical and biological contexts due to the prevalence of chiral biochemical compounds. Circular dichroism (CD) spectroscopy serves as a method for enantiomer-specific analysis of chiral samples. It is important to highlight that specific resonant nanostructures significantly amplify circular dichroism responses, thus enhancing spectroscopy and photochemistry sensitivity, and consequently elevating chiral sensing precision[261]. The theoretical exploration of BIC generation in chiral quantum systems occurred in 2014[262]. Subsequently, in 2019, Koshelev *et al.* investigated the impact of detuning between electrical and magnetic dipole resonances in silicon nano-cylinders, leading to substantial enhancement of optical chirality at the nanoscale[247]. Continuing this trajectory, Chen *et al.* in 2020 demonstrated a CD spectrum and molar concentration retrieval using an individual metasurface with high sensitivity. Utilizing the high-Q resonances, a hyperchiral field amplification of the CD signal by a factor of 59 was observed, accompanied by a substantial FOM of 80.6 for molar concentration detection[241] as shown in Fig. 14(d). Consequently, this approach emerged as a promising methodology in the food industry, medical diagnostics, and drug development.

In general, BICs can be utilized to selectively suppress or eliminate radiation to achieve ultra-high Q factors, and ultra-long-lifetime optical modes with specific phase and polarization, thus providing a flexible means for light manipulation. In addition to the applications regarding lasing and sensing mentioned above, the applications of BICs also include wavefront manipulation with nonlocal metasurfaces[263–266], photocatalytic platforms based on ultrathin reactive materials[267], ultra-low-loss grating couplers employing UGRs[268], etc.

5 Summary and Outlook

In this review, we summarize the burgeoning field of optical BICs in periodic structures. The physical mechanisms behind BICs were elucidated from different physical perspectives, covering FW BICs, plane-wave and Bloch-wave perspectives, multipolar perspectives, and the intriguing topological perspective. Diverse effects enabled by BICs were categorized and collected, encompassing evolution rules, modulation methods, quasi-BICs, and the exploitation of high Q factors for light propagation and intricate light–matter interactions. Particularly noteworthy is the revelation of topological charges carried by BICs in momentum space, opening new avenues for light manipulation. Applications of BICs in periodic structures are highlighted, with a focus on BIC lasing and sensing. The synthesis of high Q factors and topological vortex configurations in momentum space introduces unprecedented degrees of freedom for modulating light in optical systems.

During the research history of optical BICs, the optical measurement systems have played an important role and also been developed. The photonic band structures are usually used to characterize BICs. The band measurement requires the momentum-space measurement capability. The angle-resolved measurement is the usually applied method, in which the input or output angles relative to the normal direction can be converted to in-plane wave vectors. For samples with large sizes, the angle-resolved measurement can be realized by a macroscopic angle-resolved measurement system, in which the momentum-space mapping is realized by continuously changing the incident and detected angles[15], while in most works, samples are usually small (length and width are only hundreds of microns or even smaller). For microscopic cases, the momentum-space imaging method based on the Fourier transform (FT) by an optical lens is applied[269], by which the momentum-space image can be obtained with a single measurement. The FT-based method can also be applied to directly observe the iso-frequency images at a certain frequency, which can be used to characterize the momentum-space polarization vortex configurations around BICs[23,24]. Besides the photonic band measurements, the Q factor measurement is another important aspect to characterize BICs. Besides directly fitting the resonant spectra[15,23], the scattering measurements can also be applied[39,270,271], by which the Q factors can be extracted from the frequency-dependent scattering spectra. Moreover, the observations of novel phenomena enabled by BICs further require more measurement dimensions. For example, the phase measurement methods are also applied and improved to characterize the momentum-space phase modulation enabled by BICs[121,123]. For future developments, the near-field measurement methods and time-domain measurement methods may also be included to observe other novel effects enabled by BICs. Meanwhile, the optical measurement setups developed or improved in BIC studies can also be applied in other research areas such as light–matter interactions, and wavefront control based on nanostructures.

The exploration of optical BICs in periodic structures has unveiled a wealth of intriguing phenomena and practical applications. As we look to the future, several exciting directions emerge that promise to further enrich our understanding and leverage the potential of BICs.

Many physical mechanisms and various types of optical BICs have been discussed, while the possible mechanisms and types have not been covered. For instance, optical BICs are mostly discussed when the optical modes are below the diffraction limit. The cases above the diffraction limit need to be further explored. The observed topological charges of optical BICs in periodic structures are not larger than $+1$ and smaller than -2. Finding the high-order BICs and revealing the physical mechanisms beyond the symmetry perspective will help us to have a deep insight into the topological properties of optical BICs. For quasi-BICs in moiré structures and photonic quasicrystals[53,78,86], more explorations are required to establish the modulation and evolution mechanism. And there are still many degrees of freedom in multilayer compound structures constructed by periodic structures, such as the interlayer coupling[272], to be explored. When considering synthetic dimensions[273], there are more expected discoveries of new types of optical BICs.

Optical systems supporting BICs have exhibited many advantages as an ideal platform for studying light–matter interaction[274–276]. Enabled by the high Q factors of optical BICs, the interaction time between light and matter can be significantly enhanced. The improvement of nonlinear conversion efficiency has been explored, and the observed enhancement factors are obvious[82,197,277–281]. Additionally, the interaction between BICs and other quasi particles like excitons presents an exciting avenue for the investigation of light–matter interactions[148,152,162,282]. The strong-coupling-induced polaritons also

possess properties of optical BICs, leading to novel effects like new-type polariton lasing carrying topological polarization configurations[147,192]. Understanding the interplay between these phenomena could open new possibilities for controlling and manipulating light in complex optical systems. Similar to BICs, optical anapole modes also have nonradiating properties[283–285]. Examining the profound connections between anapole modes and BICs will significantly broaden the potential applications of BICs.

Furthermore, the application scope of BICs is expected to expand beyond lasing and sensing. Exploring their potential in areas such as integrated optical circuits[286] and quantum-enhanced technologies[287] will be of paramount importance. The integration of BICs with emerging technologies, such as quantum optics and information processing, holds significant promise. Exploring the synergy between BICs and quantum phenomena could lead to the development of more efficient quantum communication and computation devices.

Finally, theoretical advancements must be translated into practical, real-world applications, fostering a symbiotic relationship between fundamental understanding and technological innovation. Advances in the fabrication techniques of periodic structures will likely play a pivotal role in tailoring BICs for specific applications. In many previous experimental results, the optical BICs are actually studied in periodic structures with only tens or hundreds of periods in consideration of the cost of conventional fabrication methods like electron beam lithography. Hence many experiments are limited to being realized in microscopy systems, requiring complicated experimental setups. The low-cost and time-saving approaches to fabricating specially designed periodic structures supporting optical BICs are still in demand for easier observation and applications. Besides, with deeper insight into the modulations of optical BICs, more sophisticated three-dimensional periodic structures like tilted gratings requiring special slit angles and multilayered structures requiring precise alignment are needed to achieve special modulation effects[60,61,72,73]. There are still many theoretically proposed optical BICs with novel properties to be experimentally implemented, in which many of them are hindered by the sample preparations. The development of fabrication methods will enable the engineering of structures with unprecedented precision and speed, pushing the boundaries of application scenarios of optical BICs.

In conclusion, the outlook for optical BICs in periodic structures is promising and multifaceted. As we embark on this journey of discovery, the synergy of theoretical insights, technological advancements, and interdisciplinary collaborations will propel optical BICs to the forefront of cutting-edge optics and photonics, shaping the landscape of future optical technologies.

Acknowledgments

References

1. J. von Neumann and E. Wigner, "Über merkwürdige diskrete eigenworte," *Phys. Z* **30**, 465 (1929).
2. F. H. Stillinger and D. R. Herrick, "Bound states in the continuum," *Phys. Rev. A* **11**, 446 (1975).
3. K. Yamanouchi and K. Shibayama, "Propagation and amplification of rayleigh waves and piezoelectric leaky surface waves in linbo3," *J. Appl. Phys.* **43**, 856 (1972).
4. A. Lyapina *et al.*, "Bound states in the continuum in open acoustic resonators," *J. Fluid Mech.* **780**, 370 (2015).
5. I. Deriy *et al.*, "Bound states in the continuum in compact acoustic resonators," *Phys. Rev. Lett.* **128**, 084301 (2022).
6. Z. Zhou *et al.*, "Observation of perfectly-chiral exceptional point via bound state in the continuum," *Phys. Rev. Lett.* **130**, 116101 (2023).
7. M. McIver, "An example of non-uniqueness in the two-dimensional linear water wave problem," *J. Fluid Mech.* **315**, 257 (1996).
8. M. McIver, "Trapped modes supported by submerged obstacles," *Proc. R. Soc. A: Math. Phys. Eng. Sci.* **456**, 1851 (2000).
9. R. Porter, "Trapping of water waves by pairs of submerged cylinders," *Proc. R. Soc. A: Math. Phys. Eng. Sci.* **458**, 607 (2002).
10. C. Linton and P. McIver, "Embedded trapped modes in water waves and acoustics," *Wave Motion* **45**, 16 (2007).
11. S. Longhi, "Bound states in the continuum in a single-level fano-anderson model," *Eur. Phys. J. B* **57**, 45 (2007).
12. D. Marinica, A. Borisov, and S. Shabanov, "Bound states in the continuum in photonics," *Phys. Rev. Lett.* **100**, 183902 (2008).
13. E. N. Bulgakov and A. F. Sadreev, "Bound states in the continuum in photonic waveguides inspired by defects," *Phys. Rev. B* **78**, 075105 (2008).
14. S. Weimann *et al.*, "Compact surface fano states embedded in the continuum of waveguide arrays," *Phys. Rev. Lett.* **111**, 240403 (2013).
15. C. W. Hsu *et al.*, "Observation of trapped light within the radiation continuum," *Nature* **499**, 188 (2013).
16. C. W. Hsu *et al.*, "Bound states in the continuum," *Nat. Rev. Mater.* **1**, 1 (2016).
17. J. Gomis-Bresco, D. Artigas, and L. Torner, "Anisotropy-induced photonic bound states in the continuum," *Nat. Photonics* **11**, 232 (2017).
18. K. Koshelev, A. Bogdanov, and Y. Kivshar, "Meta-optics and bound states in the continuum," *Sci. Bull.* **64**, 836 (2019).
19. Z. Hu *et al.*, "Nonlinear control of photonic higher-order topological bound states in the continuum," *Light Sci. Appl.* **10**, 164 (2021).
20. A. F. Sadreev, "Interference traps waves in an open system: bound states in the continuum," *Rep. Prog. Phys.* **84**, 055901 (2021).
21. J. D. Joannopoulos *et al.*, *Molding the Flow of Light* (Princeton University Press, 2008).
22. B. Zhen *et al.*, "Topological nature of optical bound states in the continuum," *Phys. Rev. Lett.* **113**, 257401 (2014).
23. Y. Zhang *et al.*, "Observation of polarization vortices in momentum space," *Phys. Rev. Lett.* **120**, 186103 (2018).
24. H. M. Doeleman *et al.*, "Experimental observation of a polarization vortex at an optical bound state in the continuum," *Nat. Photonics* **12**, 397 (2018).
25. K. Koshelev *et al.*, "Asymmetric metasurfaces with high-Q resonances governed by bound states in the continuum," *Phys. Rev. Lett.* **121**, 193903 (2018).

26. H. Feshbach, "Unified theory of nuclear reactions," *Ann. Phys.* **5**, 357 (1958).

27. H. Friedrich and D. Wintgen, "Interfering resonances and bound states in the continuum," *Phys. Rev. A* **32**, 3231 (1985).

28. S. Fan, W. Suh, and J. D. Joannopoulos, "Temporal coupled-mode theory for the fano resonance in optical resonators," *J. Opt. Soc. Am. A* **20**, 569 (2003).

29. W. Suh, Z. Wang, and S. Fan, "Temporal coupled-mode theory and the presence of non-orthogonal modes in lossless multimode cavities," *IEEE J. Quantum Electron.* **40**, 1511 (2004).

30. A. Volya and V. Zelevinsky, "Non-hermitian effective hamiltonian and continuum shell model," *Phys. Rev. C* **67**, 054322 (2003).

31. M. V. Rybin *et al.*, "High-Q supercavity modes in subwavelength dielectric resonators," *Phys. Rev. Lett.* **119**, 243901 (2017).

32. S. I. Azzam *et al.*, "Formation of bound states in the continuum in hybrid plasmonic-photonic systems," *Phys. Rev. Lett.* **121**, 253901 (2018).

33. M. Kang *et al.*, "Merging bound states in the continuum at off-high symmetry points," *Phys. Rev. Lett.* **126**, 117402 (2021).

34. S. Joseph *et al.*, "Exploring the optical bound state in the continuum in a dielectric grating coupled plasmonic hybrid system," *Adv. Opt. Mater.* **9**, 2001895 (2021).

35. Y. Zhou *et al.*, "Dual-quasi bound states in the continuum enabled plasmonic metasurfaces," *Adv. Opt. Mater.* **10**, 2200965 (2022).

36. K. Sakoda, "Symmetry, degeneracy, and uncoupled modes in two-dimensional photonic lattices," *Phys. Rev. B* **52**, 7982 (1995).

37. T. Ochiai, and K. Sakoda, "Dispersion relation and optical transmittance of a hexagonal photonic crystal slab," *Phys. Rev. B* **63**, 125107 (2001).

38. J. Lee *et al.*, "Observation and differentiation of unique high-q optical resonances near zero wave vector in macroscopic photonic crystal slabs," *Phys. Rev. Lett.* **109**, 067401 (2012).

39. J. Jin *et al.*, "Topologically enabled ultrahigh-q guided resonances robust to out-of-plane scattering," *Nature* **574**, 501 (2019).

40. T. Yoda and M. Notomi, "Generation and annihilation of topologically protected bound states in the continuum and circularly polarized states by symmetry breaking," *Phys. Rev. Lett.* **125**, 053902 (2020).

41. C. F. Doiron, I. Brener, and A. Cerjan, "Realizing symmetry-guaranteed pairs of bound states in the continuum in metasurfaces," *Nat. Commun.* **13**, 7534 (2022).

42. X. Gao *et al.*, "Formation mechanism of guided resonances and bound states in the continuum in photonic crystal slabs," *Sci. Rep.* **6**, 31908 (2016).

43. X. Gao *et al.*, "Bound states in the continuum in fiber bragg gratings," *ACS Photonics* **6**, 2996 (2019).

44. P. Hu *et al.*, "Global phase diagram of bound states in the continuum," *Optica* **9**, 1353 (2022).

45. Y. Yang *et al.*, "Analytical perspective for bound states in the continuum in photonic crystal slabs," *Phys. Rev. Lett.* **113**, 037401 (2014).

46. Y. Yang *et al.*, "Three-dimensional coupled-wave theory for the guided mode resonance in photonic crystal slabs: Tm-like polarization," *Opt. Lett.* **39**, 4498 (2014).

47. S. Dai *et al.*, "From topologically protected coherent perfect reflection to bound states in the continuum," *Phys. Rev. B* **98**, 081405 (2018).

48. P. Hu *et al.*, "Bound states in the continuum based on the total internal reflection of bloch waves," *Natl. Sci. Rev.* **10**, nwac043 (2023).

49. J. D. Jackson, *Classical Electrodynamics* (1999).

50. W. Chen, Y. Chen, and W. Liu, "Singularities and poincaré indices of electromagnetic multipoles," *Phys. Rev. Lett.* **122**, 153907 (2019).

51. Z. Sadrieva *et al.*, "Multipolar origin of bound states in the continuum," *Phys. Rev. B* **100**, 115303 (2019).

52. W. Chen, Y. Chen, and W. Liu, "Line singularities and hopf indices of electromagnetic multipoles," *Laser Photonics Rev.* **14**, 2000049 (2020).

53. Z. Che *et al.*, "Polarization singularities of photonic quasicrystals in momentum space," *Phys. Rev. Lett.* **127**, 043901 (2021).

54. M. Gong *et al.*, "Multipolar perspective on unidirectional guided resonances," *Phys. Rev. A* **108**, 013522 (2023).

55. Q. Jiang *et al.*, "General bound states in the continuum in momentum space," *Phys. Rev. Lett.* **131**, 013801 (2023).

56. K. Sakoda and K. Sakoda, *Optical Properties of Photonic Crystals*, Vol. **2** (Springer, 2005).

57. X. Wang *et al.*, "Realizing tunable evolution of bound states in the continuum and circularly polarized points by symmetry breaking," *ACS Photonics* **10**, 2316 (2022).

58. E. N. Bulgakov and A. F. Sadreev, "Bloch bound states in the radiation continuum in a periodic array of dielectric rods," *Phys. Rev. A* **90**, 053801 (2014).

59. W. Ye, Y. Gao, and J. Liu, "Singular points of polarizations in the momentum space of photonic crystal slabs," *Phys. Rev. Lett.* **124**, 153904 (2020).

60. X. Yin *et al.*, "Observation of topologically enabled unidirectional guided resonances," *Nature* **580**, 467 (2020).

61. Y. Zeng *et al.*, "Dynamics of topological polarization singularity in momentum space," *Phys. Rev. Lett.* **127**, 176101 (2021).

62. M. Kang *et al.*, "Merging bound states in the continuum by harnessing higher-order topological charges," *Light Sci. Appl.* **11**, 228 (2022).

63. X. Qi *et al.*, "Steerable merging bound states in the continuum on a quasi-flatband of photonic crystal slabs without breaking symmetry," *Photonics Res.* **11**, 1262 (2023).

64. S. Wan *et al.*, "Topologically enabled ultrahigh-q chiroptical resonances by merging bound states in the continuum," *Opt. Lett.* **47**, 3291 (2022).

65. H. Luo *et al.*, "Dynamics of diverse polarization singularities in momentum space with far-field interference," *Phys. Rev. A* **107**, 013504 (2023).

66. W. Liu *et al.*, "Circularly polarized states spawning from bound states in the continuum," *Phys. Rev. Lett.* **123**, 116104 (2019).

67. J. Wang *et al.*, "Routing valley exciton emission of a WS2 monolayer via delocalized bloch modes of in-plane inversion-symmetry-broken photonic crystal slabs," *Light Sci. Appl.* **9**, 148 (2020).

68. S. Kim *et al.*, "Topological control of 2d perovskite emission in the strong coupling regime," *Nano Lett.* **21**, 10076 (2021).

69. J. Tian *et al.*, "Optical rashba effect in a light-emitting perovskite metasurface," *Adv. Mater.* **34**, 2109157 (2022).

70. X. Zhang *et al.*, "Chiral emission from resonant metasurfaces," *Science* **377**, 1215 (2022).

71. Y. Chen *et al.*, "Observation of intrinsic chiral bound states in the continuum," *Nature* **613**, 474 (2023).

72. X. Yin *et al.*, "Topological unidirectional guided resonances emerged from interband coupling," *Phys. Rev. Lett.* **130**, 056401 (2023).

73. H. Qin *et al.*, "Arbitrarily polarized bound states in the continuum with twisted photonic crystal slabs," *Light Sci. Appl.* **12**, 66 (2023).

74. Q. Song *et al.*, "Coexistence of a new type of bound state in the continuum and a lasing threshold mode induced by pt symmetry," *Sci. Adv.* **6**, eabc1160 (2020).

75. C. Zhao *et al.*, "Magnetic modulation of topological polarization singularities in momentum space," *Opt. Lett.* **47**, 2754 (2022).

76. C. Huang *et al.*, "Ultrafast control of vortex microlasers," *Science* **367**, 1018 (2020).

77. Y. Hu *et al.*, "Spatiotemporal lineshape tailoring in bic-mediated reconfigurable metamaterials," *Adv. Funct. Mater.* **32**, 2203680 (2022).

78. L. Huang, W. Zhang, and X. Zhang, "Moiré quasibound states in the continuum," *Phys. Rev. Lett.* **128**, 253901 (2022).

79. Z. Chen *et al.*, "Observation of miniaturized bound states in the continuum with ultra-high quality factors," *Sci. Bull.* **67**, 359 (2022).

80. A. Overvig, N. Yu, and A. Alù, "Chiral quasi-bound states in the continuum," *Phys. Rev. Lett.* **126**, 073001 (2021).

81. A. Tittl *et al.*, "Imaging-based molecular barcoding with pixelated dielectric metasurfaces," *Science* **360**, 1105 (2018).

82. Z. Liu *et al.*, "High-q quasibound states in the continuum for nonlinear metasurfaces," *Phys. Rev. Lett.* **123**, 253901 (2019).

83. X. Wang *et al.*, "Controlling light absorption of graphene at critical coupling through magnetic dipole quasi-bound states in the continuum resonance," *Phys. Rev. B* **102**, 155432 (2020).

84. S. Han *et al.*, "Extended bound states in the continuum with symmetry-broken terahertz dielectric metasurfaces," *Adv. Opt. Mater.* **9**, 2002001 (2021).

85. L. Kühner *et al.*, "Radial bound states in the continuum for polarization-invariant nanophotonics," *Nat. Commun.* **13**, 4992 (2022).

86. Y. Zhang *et al.*, "Unfolded band structures of photonic quasicrystals and moiré superlattices," *Phys. Rev. B* **105**, 165304 (2022).

87. H. Tang *et al.*, "On-chip light trapping in bilayer moiré photonic crystal slabs," *Appl. Phys. Lett.* **121**, 231702 (2022).

88. H. Tang *et al.*, "Experimental probe of twist angle–dependent band structure of on-chip optical bilayer photonic crystal," *Sci. Adv.* **9**, eadh8498 (2023).

89. F. Wang *et al.*, "Automatic optimization of miniaturized bound states in the continuum cavity," *Opt. Express* **31**, 123846 (2023).

90. Y. Ren *et al.*, "Low-threshold nanolasers based on miniaturized bound states in the continuum," *Sci. Adv.* **8**, eade8817 (2022).

91. H. Zhong *et al.*, "Ultra-low threshold continuous-wave quantum dot mini-BIC lasers," *Light Sci. Appl.* **12**, 100 (2023).

92. Y. Chen *et al.*, "Multidimensional nanoscopic chiroptics," *Nat. Rev. Phys.* **4**, 113 (2022).

93. M. V. Gorkunov, A. A. Antonov, and Y. S. Kivshar, "Metasurfaces with maximum chirality empowered by bound states in the continuum," *Phys. Rev. Lett.* **125**, 093903 (2020).

94. J. Dixon *et al.*, "Self-isolated raman lasing with a chiral dielectric metasurface," *Phys. Rev. Lett.* **126**, 123201 (2021).

95. J. Wu *et al.*, "Observation of giant extrinsic chirality empowered by quasi-bound states in the continuum," *Phys. Rev. Appl.* **16**, 064018 (2021).

96. M. V. Gorkunov *et al.*, "Bound states in the continuum underpin near-lossless maximum chirality in dielectric metasurfaces," *Adv. Opt. Mater.* **9**, 2100797 (2021).

97. T. Shi *et al.*, "Planar chiral metasurfaces with maximal and tunable chiroptical response driven by bound states in the continuum," *Nat. Commun.* **13**, 4111 (2022).

98. Y. Lim *et al.*, "Maximally chiral emission via chiral quasibound states in the continuum," *Laser Photonics Rev.* **17**, 2200611 (2023).

99. Y. Tang *et al.*, "Chiral bound states in the continuum in plasmonic metasurfaces," *Laser Photonics Rev.* **17**, 2200597 (2023).

100. X. Huang *et al.*, "Dirac cones induced by accidental degeneracy in photonic crystals and zero-refractive-index materials," *Nat. Mater.* **10**, 582 (2011).

101. Y. Li *et al.*, "On-chip zero-index metamaterials," *Nat. Photonics* **9**, 738 (2015).

102. M. Minkov *et al.*, "Zero-index bound states in the continuum," *Phys. Rev. Lett.* **121**, 263901 (2018).

103. H. Tang *et al.*, "Low-loss zero-index materials," *Nano Lett.* **21**, 914 (2021).

104. T. Dong *et al.*, "Ultra-low-loss on-chip zero-index materials," *Light Sci. Appl.* **10**, 10 (2021).

105. D. I. Vulis *et al.*, "Monolithic cmos-compatible zero-index metamaterials," *Opt. Express* **25**, 12381 (2017).

106. Z. Zhang *et al.*, "Negative refraction mediated by bound states in the continuum," *Photonics Res.* **9**, 1592 (2021).

107. S. Lepeshov, M. Yesmantovich, and A. Bogdanov, "Topological enhancement of evanescent field localization in all-dielectric metasurfaces," *Optica* **10**, 797 (2023).

108. S. Yang *et al.*, "Nanoparticle trapping in a quasi-BIC system," *ACS Photonics* **8**, 1961 (2021).

109. Y. Shi *et al.*, "Multifunctional virus manipulation with large-scale arrays of all-dielectric resonant nanocavities," *Laser Photonics Rev.* **16**, 2100197 (2022).

110. E. Bulgakov and A. Sadreev, "Precise size sorting of nanoparticles by bound states in the continuum in a dual finite grating," *Opt. Lett.* **48**, 4705 (2023).

111. S. Yang and J. C. Ndukaife, "Optofluidic transport and assembly of nanoparticles using an all-dielectric quasi-BIC metasurface," *Light Sci. Appl.* **12**, 188 (2023).

112. Z. Dong *et al.*, "Schrödinger's red pixel by quasi-bound-states-in-the-continuum," *Sci. Adv.* **8**, eabm4512 (2022).

113. F. Wu *et al.*, "Giant enhancement of the goos-hänchen shift assisted by quasibound states in the continuum," *Phys. Rev. Appl.* **12**, 014028 (2019).

114. M. Liu and D.-Y. Choi, "Extreme huygens' metasurfaces based on quasi-bound states in the continuum," *Nano Lett.* **18**, 8062 (2018).

115. Y. Li *et al.*, "A platform for integrated spectrometers based on solution-processable semiconductors," *Light Sci. Appl.* **12**, 184 (2023).

116. F. Goos and H. Hänchen, "Ein neuer und fundamentaler versuch zur totalreflexion," *Ann. Phys.* **436**, 333 (1947).

117. L.-G. Wang, H. Chen, and S.-Y. Zhu, "Large negative goos–hänchen shift from a weakly absorbing dielectric slab," *Opt. Lett.* **30**, 2936 (2005).

118. L.-G. Wang and S.-Y. Zhu, "Giant lateral shift of a light beam at the defect mode in one-dimensional photonic crystals," *Opt. Lett.* **31**, 101 (2006).

119. J. Wang *et al.*, "Shifting beams at normal incidence via controlling momentum-space geometric phases," *Nat. Commun.* **12**, 6046 (2021).

120. S. Du *et al.*, "Realization of large transmitted goos–hänchen shifts with high (near 100%) transmittance based on a coupled double-layer grating system," *Opt. Lett.* **48**, 1710 (2023).

121. B. Wang *et al.*, "Generating optical vortex beams by momentum-space polarization vortices centred at bound states in the continuum," *Nat. Photonics* **14**, 623 (2020).

122. W. Liu *et al.*, "Ways to achieve efficient non-local vortex beam generation," *Nanophotonics* **10**, 4297 (2021).

123. T. Li *et al.*, "High-efficiency nonlocal reflection-type vortex beam generation based on bound states in the continuum," *Natl. Sci. Rev.* **10**, nwac234 (2023).

124. L. Kang *et al.*, "High-harmonic optical vortex generation from photonic bound states in the continuum," *Adv. Opt. Mater.* **10**, 2101497 (2022).

125. M. Notomi, "Topology in momentum space becomes real," *Nat. Photonics* **14**, 595 (2020).

126. J. Wang, L. Shi and J. Zi, "Spin hall effect of light via momentum-space topological vortices around bound states in the continuum," *Phys. Rev. Lett.* **129**, 236101 (2022).

127. M. Kang *et al.*, "Coherent full polarization control based on bound states in the continuum," *Nat. Commun.* **13**, 4536 (2022).

128. H. Qin *et al.*, "Exploiting extraordinary topological optical forces at bound states in the continuum," *Sci. Adv.* **8**, eade7556 (2022).

129. K. Y. Bliokh *et al.*, "Spin–orbit interactions of light," *Nat. Photonics* **9**, 796 (2015).

130. Y. Guo, M. Xiao, and S. Fan, "Topologically protected complete polarization conversion," *Phys. Rev. Lett.* **119**, 167401 (2017).

131. Y. Guo *et al.*, "Arbitrary polarization conversion with a photonic crystal slab," *Adv. Opt. Mater.* **7**, 1801453 (2019).

132. F. Chen *et al.*, "Observation of topologically enabled complete polarization conversion," *Laser Photonics Rev.* **17**, 2200626 (2023).

133. H. J. Kimble, "The quantum internet," *Nature* **453**, 1023 (2008).
134. M. S. Tame *et al.*, "Quantum plasmonics," *Nat. Phys.* **9**, 329 (2013).
135. O. Benson, "Assembly of hybrid photonic architectures from nanophotonic constituents," *Nature* **480**, 193 (2011).
136. Z. Qian *et al.*, "Spontaneous emission in micro-or nanophotonic structures," *PhotoniX* **2**, 1 (2021).
137. A. Rahimi-Iman, *Polariton Physics* (Springer International Publishing, 2020).
138. C. Cohen-Tannoudji and S. Reynaud, "Dressed-atom description of resonance fluorescence and absorption spectra of a multi-level atom in an intense laser beam," *J. Phys. B* **10**, 345 (1977).
139. P. Meystre and M. Sargent, *Elements of Quantum Optics* (Springer Science and Business Media, 2007).
140. A. Amo and J. Bloch, "Exciton-polaritons in lattices: a non-linear photonic simulator," *C.R. Phys.* **17**, 934 (2016).
141. D. Sanvitto and S. Kéna-Cohen, "The road towards polaritonic devices," *Nat. Mater.* **15**, 1061 (2016).
142. K. Daskalakis *et al.*, "Nonlinear interactions in an organic polariton condensate," *Nat. Mater.* **13**, 271 (2014).
143. M. Skolnick, T. Fisher, and D. Whittaker, "Strong coupling phenomena in quantum microcavity structures," *Semicond. Sci. Technol.* **13**, 645 (1998).
144. R. Tao *et al.*, "Room-temperature observation of trapped exciton-polariton emission in GaN/AlGaN microcavities with air-gap/iii-nitride distributed bragg reflectors," *ACS Photonics* **3**, 1182 (2016).
145. F. Wang *et al.*, "Fundamentals and applications of topological polarization singularities," *Front. Phys.* **10**, 198 (2022).
146. J. Bloch *et al.*, "Strongly correlated electron–photon systems," *Nature* **606**, 41 (2022).
147. V. Ardizzone *et al.*, "Polariton Bose–Einstein condensate from a bound state in the continuum," *Nature* **605**, 447 (2022).
148. E. Maggiolini *et al.*, "Strongly enhanced light–matter coupling of monolayer WS2 from a bound state in the continuum," *Nat. Mater.* **22**, 964 (2023).
149. Y. Wang *et al.*, "Directional emission from electrically injected exciton–polaritons in perovskite metasurfaces," *Nano Lett.* **23**, 4431 (2023).
150. P. Lodahl, S. Mahmoodian, and S. Stobbe, "Interfacing single photons and single quantum dots with photonic nanostructures," *Rev. Mod. Phys.* **87**, 347 (2015).
151. K. Koshelev *et al.*, "Strong coupling between excitons in transition metal dichalcogenides and optical bound states in the continuum," *Phys. Rev. B* **98**, 161113 (2018).
152. V. Kravtsov *et al.*, "Nonlinear polaritons in a monolayer semiconductor coupled to optical bound states in the continuum," *Light Sci. Appl.* **9**, 56 (2020).
153. S. Cao *et al.*, "Normal-incidence-excited strong coupling between excitons and symmetry-protected quasi-bound states in the continuum in silicon nitride–ws2 heterostructures at room temperature," *J. Phys. Chem. Lett.* **11**, 4631 (2020).
154. I. A. Al-Ani *et al.*, "Enhanced strong coupling of TMDC monolayers by bound state in the continuum," *Laser Photonics Rev.* **15**, 2100240 (2021).
155. J. Wu and Y. M. Qing, "Strong coupling of excitons in patterned few-layer WS$_2$ with guided mode and bound state in the continuum," *Phys. Chem. Chem. Phys.* **24**, 233820 (2022).
156. M. Qin *et al.*, "Strong coupling between excitons and magnetic dipole quasi-bound states in the continuum in WS$_2$-TiO$_2$ hybrid metasurfaces," *Opt. Express* **29**, 180266 (2021).
157. M. Qin *et al.*, "Strong coupling between excitons and quasibound states in the continuum in bulk transition metal dichalcogenides," *Phys. Rev. B* **107**, 045417 (2023).
158. P. Xie *et al.*, "Strong coupling between excitons in a two-dimensional atomic crystal and quasibound states in the continuum in a two-dimensional all-dielectric asymmetric metasurface," *Phys. Rev. B* **104**, 125446 (2021).
159. X. Gu *et al.*, "Polaritonic coherent perfect absorption based on self-hybridization of a quasi-bound state in the continuum and exciton," *Opt. Express* **31**, 4691 (2023).
160. X. Zong *et al.*, "Enhanced light–matter interactions in ultrathin transition-metal-dichalcogenide metasurfaces by magnetic and toroidal dipole bound states in the continuum," *Opt. Express* **30**, 431047 (2022).
161. P. Xie *et al.*, "Cavity-assisted boosting of self-hybridization between excitons and photonic bound states in the continuum in multilayers of transition metal dichalcogenides," *Phys. Rev. B* **107**, 075415 (2023).
162. T. Weber *et al.*, "Intrinsic strong light–matter coupling with self-hybridized bound states in the continuum in van der Waals metasurfaces," *Nat. Mater.* **22**, 970 (2023).
163. L. Lu *et al.*, "Engineering a light–matter strong coupling regime in perovskite-based plasmonic metasurface: quasi-bound state in the continuum and exceptional points," *Photonics Res.* **8**, A91–A100 (2020).
164. I. A. Al-Ani *et al.*, "Strong coupling of exciton and high-q mode in all-perovskite metasurfaces," *Adv. Opt. Mater.* **10**, 2101120 (2022).
165. X. Xu and S. Jin, "Strong coupling of single quantum dots with low-refractive-index/high-refractive-index materials at room temperature," *Sci. Adv.* **6**, eabb3095 (2020).
166. Z. Zhen *et al.*, "Strong coupling between colloidal quantum dots and a microcavity with hybrid structure at room temperature," *Photonics Res.* **10**, 913 (2022).
167. D. Bosomtwi and V. E. Babicheva, "Beyond conventional sensing: Hybrid plasmonic metasurfaces and bound states in the continuum," *Nanomaterials* **13**, 1261 (2023).
168. K. Sun *et al.*, "Strong coupling between quasi-bound states in the continuum and molecular vibrations in the mid-infrared," *Nanophotonics* **11**, 4221 (2022).
169. A. A. Bogdanov *et al.*, "Bound states in the continuum and fano resonances in the strong mode coupling regime," *Adv. Photonics* **1**, 1 (2019).
170. N. Solodovchenko *et al.*, "Bound states in the continuum in strong-coupling and weak-coupling regimes under the cylinder–ring transition," *Nanophotonics* **10**, 4347 (2021).
171. P. Xie *et al.*, "Tunable interactions of quasibound states in the continuum with cavity mode in a metasurface-microcavity hybrid," *Phys. Rev. B* **106**, 165408 (2022).
172. A. Imamog *et al.*, "Nonequilibrium condensates and lasers without inversion: Exciton-polariton lasers," *Phys. Rev. A* **53**, 4250 (1996).
173. S. Pau *et al.*, "Observation of a laserlike transition in a microcavity exciton polariton system," *Phys. Rev. A* **54**, R1789 (1996).
174. J. Kasprzak *et al.*, "Bose–Einstein condensation of exciton polaritons," *Nature* **443**, 409 (2006).
175. C. Schneider *et al.*, "An electrically pumped polariton laser," *Nature* **497**, 348 (2013).
176. H. Deng, H. Haug, and Y. Yamamoto, "Exciton-polariton Bose–Einstein condensation," *Rev. Mod. Phys.* **82**, 1489 (2010).
177. I. Carusotto and C. Ciuti, "Quantum fluids of light," *Rev. Mod. Phys.* **85**, 299 (2013).
178. T. Byrnes, N. Y. Kim, and Y. Yamamoto, "Exciton–polariton condensates," *Nat. Phys.* **10**, 803 (2014).
179. L. Kappei *et al.*, "Direct observation of the Mott transition in an optically excited semiconductor quantum well," *Phys. Rev. Lett.* **94**, 147403 (2005).
180. N. Mott, *Metal-Insulator Transitions* (CRC Press, 2004).
181. A. Rahimi-Iman, *Nichtlineare Effekte in III/V Quantenfilm-Mikroresonatoren: Von dynamischer Bose-Einstein-Kondensation hin zum elektrisch betriebenen Polariton-Laser* (Cuvillier, 2013).
182. J. D. Plumhof *et al.*, "Room-temperature Bose–Einstein condensation of cavity exciton–polaritons in a polymer," *Nat. Mater.* **13**, 247 (2014).

183. S. Utsunomiya *et al.*, "Observation of Bogoliubov excitations in exciton-polariton condensates," *Nat. Phys.* **4**, 700 (2008).

184. X. Wu *et al.*, "Room-temperature bound states in the continuum polariton condensation," arXiv:2303.09923 (2023).

185. M. Amthor *et al.*, "Electro-optical switching between polariton and cavity lasing in an InGaAs quantum well microcavity," *Opt. Express* **22**, 31146 (2014).

186. H. Deng *et al.*, "Condensation of semiconductor microcavity exciton polaritons," *Science* **298**, 199 (2002).

187. M. Richard *et al.*, "Spontaneous coherent phase transition of polaritons in CdTe microcavities," *Phys. Rev. Lett.* **94**, 187401 (2005).

188. S. Christopoulos *et al.*, "Room-temperature polariton lasing in semiconductor microcavities," *Phys. Rev. Lett.* **98**, 126405 (2007).

189. F. Li *et al.*, "From excitonic to photonic polariton condensate in a ZnO-based microcavity," *Phys. Rev. Lett.* **110**, 196406 (2013).

190. R. Su *et al.*, "Room-temperature polariton lasing in all-inorganic perovskite nanoplatelets," *Nano Lett.* **17**, 3982 (2017).

191. S. Dufferwiel *et al.*, "Exciton–polaritons in van der Waals heterostructures embedded in tunable microcavities," *Nat. Commun.* **6**, 8579 (2015).

192. A. M. Berghuis *et al.*, "Room temperature exciton–polariton condensation in silicon metasurfaces emerging from bound states in the continuum," *Nano Lett.* **23**, 5603 (2023).

193. L. Carletti *et al.*, "Giant nonlinear response at the nanoscale driven by bound states in the continuum," *Phys. Rev. Lett.* **121**, 033903 (2018).

194. K. Koshelev *et al.*, "Subwavelength dielectric resonators for nonlinear nanophotonics," *Science* **367**, 288 (2020).

195. J. Wang *et al.*, "Doubly resonant second-harmonic generation of a vortex beam from a bound state in the continuum," *Optica* **7**, 1126 (2020).

196. T. Santiago-Cruz *et al.*, "Resonant metasurfaces for generating complex quantum states," *Science* **377**, 991 (2022).

197. Z. Liu *et al.*, "Giant enhancement of continuous wave second harmonic generation from few-layer gase coupled to high-q quasi bound states in the continuum," *Nano Lett.* **21**, 7405 (2021).

198. L. Xu *et al.*, "Dynamic nonlinear image tuning through magnetic dipole quasi-BIC ultrathin resonators," *Adv. Sci.* **6**, 1802119 (2019).

199. K.-H. Kim and J.-R. Kim, "High-q chiroptical resonances by quasi-bound states in the continuum in dielectric metasurfaces with simultaneously broken in-plane inversion and mirror symmetries," *Adv. Opt. Mater.* **9**, 2101162 (2021).

200. K. Koshelev *et al.*, "Nonlinear metasurfaces governed by bound states in the continuum," *ACS Photonics* **6**, 1639 (2019).

201. M. Imada *et al.*, "Coherent two-dimensional lasing action in surface-emitting laser with triangular-lattice photonic crystal structure," *Appl. Phys. Lett.* **75**, 316 (1999).

202. Y. Kurosaka *et al.*, "On-chip beam-steering photonic-crystal lasers," *Nat. Photonics* **4**, 447 (2010).

203. C. Peng *et al.*, "Three-dimensional coupled-wave theory analysis of a centered-rectangular lattice photonic crystal laser with a transverse-electric-like mode," *Phys. Rev. B* **86**, 035108 (2012).

204. K. Ishizaki, M. De Zoysa, and S. Noda, "Progress in photonic-crystal surface-emitting lasers," *Photonics* **6**, 96 (2019).

205. D. Ohnishi *et al.*, "Room temperature continuous wave operation of a surface-emitting two-dimensional photonic crystal diode laser," *Opt. Express* **12**, 1562 (2004).

206. E. Miyai *et al.*, "Lasers producing tailored beams," *Nature* **441**, 946 (2006).

207. H. Matsubara *et al.*, "Gan photonic-crystal surface-emitting laser at blue-violet wavelengths," *Science* **319**, 445 (2008).

208. K. Hirose *et al.*, "Watt-class high-power, high-beam-quality photonic-crystal lasers," *Nat. Photonics* **8**, 406 (2014).

209. M. Yoshida *et al.*, "Double-lattice photonic-crystal resonators enabling high-brightness semiconductor lasers with symmetric narrow-divergence beams," *Nat. Mater.* **18**, 121 (2019).

210. R. Morita *et al.*, "Photonic-crystal lasers with two-dimensionally arranged gain and loss sections for high-peak-power short-pulse operation," *Nat. Photonics* **15**, 311 (2021).

211. R. Sakata *et al.*, "Dually modulated photonic crystals enabling high-power high-beam-quality two-dimensional beam scanning lasers," *Nat. Commun.* **11**, 3487 (2020).

212. M. Yoshida *et al.*, "High-brightness scalable continuous-wave single-mode photonic-crystal laser," *Nature* **618**, 727 (2023).

213. S. T. Ha *et al.*, "Directional lasing in resonant semiconductor nanoantenna arrays," *Nat. Nanotechnol.* **13**, 1042 (2018).

214. M.-S. Hwang *et al.*, "Ultralow-threshold laser using super-bound states in the continuum," *Nat. Commun.* **12**, 4135 (2021).

215. A. Kodigala *et al.*, "Lasing action from photonic bound states in continuum," *Nature* **541**, 196 (2017).

216. R. Contractor *et al.*, "Scalable single-mode surface-emitting laser via open-dirac singularities," *Nature* **608**, 692 (2022).

217. M. Wu *et al.*, "Room-temperature lasing in colloidal nanoplatelets via mie-resonant bound states in the continuum," *Nano Lett.* **20**, 6005 (2020).

218. K. Rong *et al.*, "Spin-valley rashba monolayer laser," *Nat. Mater.* **22**, 1085 (2023).

219. Y. Chen *et al.*, "Compact spin-valley-locked perovskite emission," *Nat. Mater.* **22**, 1065 (2023).

220. W. Liu *et al.*, "All-optical tuning of fano resonance for quasi-BIC and terahertz sensing applications," *Appl. Sci.* **12**, 4207 (2022).

221. W. Chen *et al.*, "Dual-resonance sensing for environmental refractive index based on quasi-BIC states in all-dielectric metasurface," *Nanophotonics* **12**, 1147 (2023).

222. B. Duan *et al.*, "High-Q quasi-BIC in photonic crystal nanobeam for ultrahigh sensitivity refractive index sensing," *Results Phys.* **47**, 106304 (2023).

223. T. C. Tan *et al.*, "Active control of nanodielectric-induced THz quasi-BIC in flexible metasurfaces: a platform for modulation and sensing," *Adv. Mater.* **33**, 2100836 (2021).

224. X. Liu *et al.*, "Terahertz metasurfaces based on bound states in the continuum (BIC) for high-sensitivity refractive index sensing," *Optik* **261**, 169248 (2022).

225. Z. Li *et al.*, "Ultrasensitive terahertz sensing in all-dielectric asymmetric metasurfaces based on quasi-BIC," *J Opt. Soc. Am. B* **39**, 286 (2022).

226. Y. Wang *et al.*, "Ultrasensitive terahertz sensing with high-Q toroidal dipole resonance governed by bound states in the continuum in all-dielectric metasurface," *Nanophotonics* **10**, 1295 (2021).

227. J. Wang *et al.*, "Quasi- BIC-governed light absorption of mono-layer transition-metal dichalcogenide-based absorber and its sensing performance," *J. Phys. D* **54**, 485106 (2021).

228. J. Zhao, L. Zhang, and Y. Li, "Superior terahertz sensing metasurface based on ultrahigh-Q toroidal dipole governed by quasi-BIC," *Europhys. Lett.* **139**, 55001 (2022).

229. X. Tu *et al.*, "Ultrahigh Q polymer microring resonators for biosensing applications," *IEEE Photonics J.* **11**, 4200110 (2019).

230. Y.-F. Xiao *et al.*, "High-Q exterior whispering-gallery modes in a metal-coated microresonator," *Phys. Rev. Lett.* **105**, 153902 (2010).

231. W.-C. Lai *et al.*, "Slow light enhanced sensitivity of resonance modes in photonic crystal biosensors," *Appl. Phys. Lett.* **102**, 041111 (2013).

232. C. Nicolaou *et al.*, "Enhanced detection limit by dark mode perturbation in 2d photonic crystal slab refractive index sensors," *Opt. Express* **21**, 31698 (2013).

233. M. Lee and P. M. Fauchet, "Two-dimensional silicon photonic crystal based biosensing platform for protein detection," *Opt. Express* **15**, 4530 (2007).

234. S. Wang *et al.*, "Optofluidic fano resonance photonic crystal refractometric sensors," *Appl. Phys. Lett.* **110**, 091105 (2017).

235. C. Kang *et al.*, "Photonic crystal slab sensor with enhanced surface area," *Opt. Express* **18**, 279307 (2010).
236. M. Huang *et al.*, "Sub-wavelength nanofluidics in photonic crystal sensors," *Opt. Express* **17**, 242243 (2009).
237. D. Dorfner *et al.*, "Photonic crystal nanostructures for optical biosensing applications," *Biosens. Bioelectron.* **24**, 3688 (2009).
238. A. Leitis *et al.*, "Angle-multiplexed all-dielectric metasurfaces for broadband molecular fingerprint retrieval," *Sci. Adv.* **5**, eaaw2871 (2019).
239. Y. Jahani *et al.*, "Imaging-based spectrometer-less optofluidic biosensors based on dielectric metasurfaces for detecting extracellular vesicles," *Nat. Commun.* **12**, 3246 (2021).
240. H.-H. Hsiao *et al.*, "Ultrasensitive refractive index sensing based on the quasi-bound states in the continuum of all-dielectric metasurfaces," *Adv. Opt. Mater.* **10**, 2200812 (2022).
241. Y. Chen *et al.*, "Integrated molar chiral sensing based on high-q metasurface," *Nano Lett.* **20**, 8696 (2020).
242. W. Cen *et al.*, "High-q fano terahertz resonance based on bound states in the continuum in all-dielectric metasurface," *Appl. Surf. Sci.* **575**, 151723 (2022).
243. W. Cen *et al.*, "Ultrasensitive flexible terahertz plasmonic metasurface sensor based on bound states in the continuum," *IEEE Sens. J.* **22**, 12838 (2022).
244. R. Ahmed *et al.*, "Large-scale functionalized metasurface-based SARS-CoV-2 detection and quantification," *ACS Nano* **16**, 159468 (2022).
245. S. Romano *et al.*, "Tuning the exponential sensitivity of a bound-state-in-continuum optical sensor," *Opt. Express* **27**, 18776 (2019).
246. J. Lv *et al.*, "High-sensitive refractive index sensing enabled by topological charge evolution," *IEEE Photonics J.* **12**, 4501610 (2020).
247. K. Koshelev *et al.*, "Enhanced circular dichroism and chiral sensing with bound states in the continuum," in *CLEO: QELS_ Fundamental Science* (2019), FTh4C–6.
248. Y. Hu *et al.*, "Quasi-bound states in the continuum enabled strong terahertz chiroptical response in bilayer metallic metasurfaces," *Crystals* **12**, 1052 (2022).
249. W. Heiss, "Repulsion of resonance states and exceptional points," *Phys. Rev. E* **61**, 929 (2000).
250. C. Dembowski *et al.*, "Experimental observation of the topological structure of exceptional points," *Phys. Rev. Lett.* **86**, 787 (2001).
251. S.-B. Lee *et al.*, "Observation of an exceptional point in a chaotic optical microcavity," *Phys. Rev. Lett.* **103**, 134101 (2009).
252. W. Chen *et al.*, "Exceptional points enhance sensing in an optical microcavity," *Nature* **548**, 192 (2017).
253. F. Yesilkoy *et al.*, "Ultrasensitive hyperspectral imaging and biodetection enabled by dielectric metasurfaces," *Nat. Photonics* **13**, 390 (2019).
254. M. Meudt *et al.*, "Hybrid photonic–plasmonic bound states in continuum for enhanced light manipulation," *Adv. Opt. Mater.* **8**, 2000898 (2020).
255. D. Yang *et al.*, "Design of simultaneous high-Q and high-sensitivity photonic crystal refractive index sensors," *J. Opt. Soc. Am. B* **30**, 2027 (2013).
256. A. Di Falco, L. O'faolain, and T. Krauss, "Chemical sensing in slotted photonic crystal heterostructure cavities," *Appl. Phys. Lett.* **94**, 063503 (2009).
257. S. Romano *et al.*, "Optical biosensors based on photonic crystals supporting bound states in the continuum," *Materials* **11**, 526 (2018).
258. S. Romano *et al.*, "Ultrasensitive surface refractive index imaging based on quasi-bound states in the continuum," *ACS Nano* **14**, 15417 (2020).
259. H. Altug *et al.*, "Advances and applications of nanophotonic biosensors," *Nat. Nanotechnol.* **17**, 5 (2022).
260. M. L. Tseng *et al.*, "Dielectric metasurfaces enabling advanced optical biosensors," *ACS Photonics* **8**, 47 (2020).
261. M. L. Solomon *et al.*, "Nanophotonic platforms for chiral sensing and separation," *Acc. Chem. Res.* **53**, 588 (2020).
262. J. Mur-Petit and R. A. Molina, "Chiral bound states in the continuum," *Phys. Rev. B* **90**, 035434 (2014).
263. A. C. Overvig, S. C. Malek, and N. Yu, "Multifunctional nonlocal metasurfaces," *Phys. Rev. Lett.* **125**, 017402 (2020).
264. S. C. Malek *et al.*, "Multifunctional resonant wavefront-shaping meta-optics based on multilayer and multi-perturbation nonlocal metasurfaces," *Light Sci. Appl.* **11**, 246 (2022).
265. Y. Zhou *et al.*, "Multiresonant nonlocal metasurfaces," *Nano Lett.* **23**, 1530 (2023).
266. A. C. Overvig *et al.*, "Zone-folded quasi-bound state metasurfaces with customized, symmetry-protected energy-momentum relations," *ACS Photonics* **10**, 1832 (2023).
267. H. Hu *et al.*, "Catalytic metasurfaces empowered by bound states in the continuum," *ACS Nano* **16**, 130578 (2022).
268. H. Wang *et al.*, "Ultra-low-loss optical interconnect enabled by topological unidirectional guided resonance," arXiv:2306.09027 (2023).
269. Y. Zhang *et al.*, "Momentum-space imaging spectroscopy for the study of nanophotonic materials," *Sci. Bull.* **66**, 824 (2021).
270. L. Shi *et al.*, "Direct observation of iso-frequency contour of surface modes in defective photonic crystals in real space," *Appl. Phys. Lett.* **97**, 251111 (2010).
271. E. C. Regan *et al.*, "Direct imaging of isofrequency contours in photonic structures," *Sci. Adv.* **2**, e1601591 (2016).
272. T. Zhang *et al.*, "Twisted moiré photonic crystal enabled optical vortex generation through bound states in the continuum," *Nat. Commun.* **14**, 6014 (2023).
273. L. Yuan *et al.*, "Synthetic dimension in photonics," *Optica* **5**, 1396 (2018).
274. P. Forn-Díaz *et al.*, "Ultrastrong coupling regimes of light–matter interaction," *Rev. Mod. Phys.* **91**, 025005 (2019).
275. N. Rivera and I. Kaminer, "Light–matter interactions with photonic quasiparticles," *Nat. Rev. Phys.* **2**, 538 (2020).
276. A. Aigner *et al.*, "Plasmonic bound states in the continuum to tailor light–matter coupling," *Sci. Adv.* **8**, eadd4816 (2022).
277. A. P. Anthur *et al.*, "Continuous wave second harmonic generation enabled by quasi-bound-states in the continuum on gallium phosphide metasurfaces," *Nano Lett.* **20**, 8745 (2020).
278. I. S. Sinev *et al.*, "Observation of ultrafast self-action effects in quasi- BIC resonant metasurfaces," *Nano Lett.* **21**, 8848 (2021).
279. G. Yang *et al.*, "Optical bound states in the continuum enabled by magnetic resonances coupled to a mirror," *Nano Lett.* **22**, 2001 (2022).
280. L. Qu *et al.*, "Giant second harmonic generation from membrane metasurfaces," *Nano Lett.* **22**, 9652 (2022).
281. X. Zhang *et al.*, "Quasi-bound states in the continuum enhanced second-harmonic generation in thin-film lithium niobate," *Laser Photonics Rev.* **16**, 2200031 (2022).
282. A. Grudinina *et al.*, "Collective excitations of a bound-in-the-continuum condensate," *Nat. Commun.* **14**, 3464 (2023).
283. A. E. Miroshnichenko *et al.*, "Nonradiating anapole modes in dielectric nanoparticles," *Nat. Commun.* **6**, 8069 (2015).
284. W. Liu, J. Zhang, and A. E. Miroshnichenko, "Toroidal dipole-induced transparency in core–shell nanoparticles," *Laser Photonics Rev.* **9**, 564 (2015).
285. K. Koshelev *et al.*, "Nonradiating photonics with resonant dielectric nanostructures," *Nanophotonics* **8**, 725 (2019).
286. Z. Yu *et al.*, "Photonic integrated circuits with bound states in the continuum," *Optica* **6**, 1342 (2019).
287. A. S. Solntsev, G. S. Agarwal, and Y. S. Kivshar, "Metasurfaces for quantum photonics," *Nat. Photonics* **15**, 327 (2021).